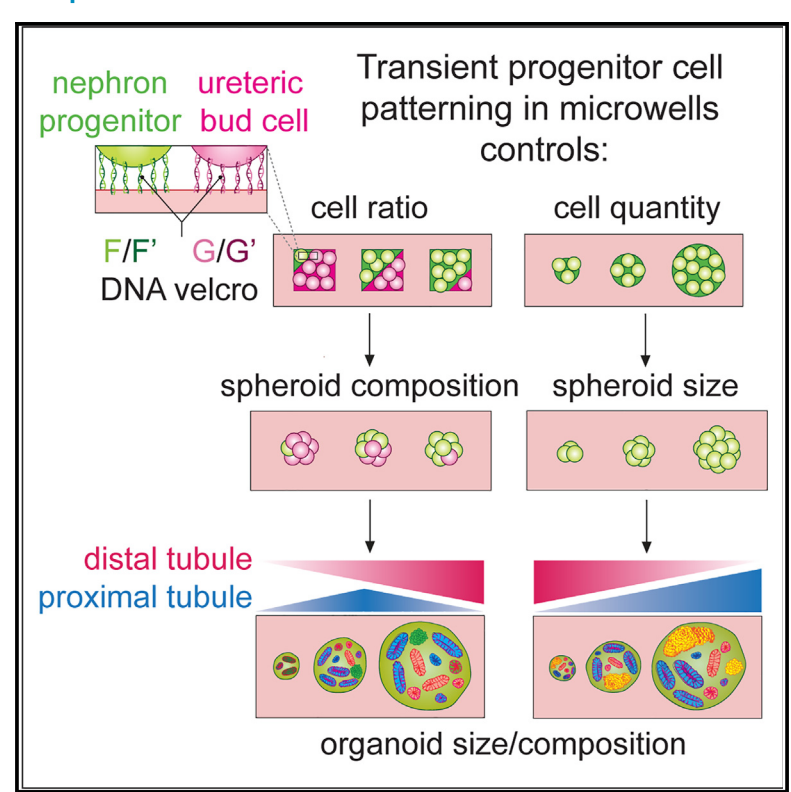
## **Cell Systems**

# Highly parallel production of designer organoids by mosaic patterning of progenitors

#### **Graphical abstract**



#### **Authors**

Catherine M. Porter, Grace C. Qian, Samuel H. Grindel, Alex J. Hughes

#### Correspondence

ajhughes@seas.upenn.edu

#### In brief

Organ formation depends on close communication among different cell types, which is open to engineering control in organoid models. Using a DNA-based cell patterning technology, we demonstrate that precise control over the initial numbers and ratios of epithelial progenitors modulates tissue composition and morphology in a human kidney organoid example.

#### **Highlights**

- Orthogonal DNA sequences precisely pattern multiple cell types within microwells
- Patterned kidney progenitors transition to 3D for long-term organoid differentiation
- Initial kidney progenitor number/ratio modulates organoid morphology and composition





## **Cell Systems**



#### Report

# Highly parallel production of designer organoids by mosaic patterning of progenitors

Catherine M. Porter, 1,2,4,5,7 Grace C. Qian, 1,2 Samuel H. Grindel, 1,2,4,5,6,7 and Alex J. Hughes 1,2,3,4,5,6,7,8,\*

#### **SUMMARY**

Organoids derived from human stem cells are a promising approach for disease modeling, regenerative medicine, and fundamental research. However, organoid variability and limited control over morphological outcomes remain as challenges. One open question is the extent to which engineering control over culture conditions can guide organoids to specific compositions. Here, we extend a DNA "velcro" cell patterning approach, precisely controlling the number and ratio of human induced pluripotent stem cell-derived progenitors contributing to nephron progenitor (NP) organoids and mosaic NP/ureteric bud (UB) tip cell organoids within arrays of microwells. We demonstrate long-term control over organoid size and morphology, decoupled from geometric constraints. We then show emergent trends in organoid tissue proportions that depend on initial progenitor cell composition. These include higher nephron and stromal cell representation in mosaic NP/UB organoids vs. NP-only organoids and a "goldilocks" initial cell ratio in mosaic organoids that optimizes the formation of proximal tubule structures.

#### **INTRODUCTION**

Kidneys are structurally and compositionally complex organs that remove waste, maintain fluid and biochemical homeostasis, and produce hormones with diverse functions. Kidney organoids derived from human induced pluripotent stem cells (hiPSCs) offer an in vitro means of modeling kidney development and disease, conducting drug and genetic screens, and producing renal replacement tissue. 2-6 Long-term, the generation of fully functional tissues for transplantation could benefit the 1 in 10 people globally who suffer from kidney disease. To date, many of the more than 26 renal cell types have been differentiated in kidney organoids. 3,4,8-16 Additionally, self-organization alone of differentiating kidney progenitors is capable of creating proximal-to-distal segmentation of nephrons and some branching morphogenesis of ureteric bud (UB) epithelium (the future urinary collection network). 13,17-20 However, the application of kidney organoids for renal replacement therapy has been hindered by several major roadblocks, such as limited organoid production scale, reproducibility, physiologic structure, connectivity, and functionality.<sup>21</sup> Deficits in organoids include insufficient branching of the collecting duct tree, incomplete fusion between UB tips and functional nephrons, and the absence of a single urinary exit path.<sup>22</sup>

Variability in kidney organoids also poses a barrier to their implementation in drug, phenotypic, and toxicological screens.<sup>23</sup> Prior studies predominantly characterized limited reproducibility between batches and in organoids derived from different stem cell lines. 16,24-27 However, variation in morphogenetic patterning, even within batches, highlights the need to standardize local microenvironments and circumvent limitations in self-assembly outcomes that contribute to unpredictable organization of tissue types within organoids.<sup>23</sup> The inherent complexity of the kidney, both structurally and compositionally, is likely a major factor contributing to this variability. For example, mimicking kidney structure and organization in organoids will require the contribution of several progenitor cell populations, which arise from different spatiotemporal origins in vivo, 4,17,18,28-30 whereas, e.g., gut organoids produce high cell diversity and crypt organization from a single Lgr5+ population.31

Previous approaches to mitigate organoid limitations have focused on controlling biochemical signaling. 3,10,19,26 However, their modest success motivates new modes of engineering control over other factors, such as initial cell population size, multiprogenitor composition, and boundary conditions, 19,32,33 with advantages recently emerging. 2,5,6,11,33 Several studies have demonstrated that controlling size and spatial characteristics



<sup>&</sup>lt;sup>1</sup>Department of Bioengineering, University of Pennsylvania, Philadelphia, PA 19104, USA

<sup>&</sup>lt;sup>2</sup>Bioengineering Graduate Group, University of Pennsylvania, Philadelphia, PA 19104, USA

<sup>&</sup>lt;sup>3</sup>Department of Cell and Developmental Biology, University of Pennsylvania, Philadelphia, PA 19104, USA

<sup>&</sup>lt;sup>4</sup>Center for Soft and Living Matter, University of Pennsylvania, Philadelphia, PA 19104, USA

<sup>&</sup>lt;sup>5</sup>Center for Precision Engineering for Health (CPE4H), University of Pennsylvania, Philadelphia, PA 19104, USA

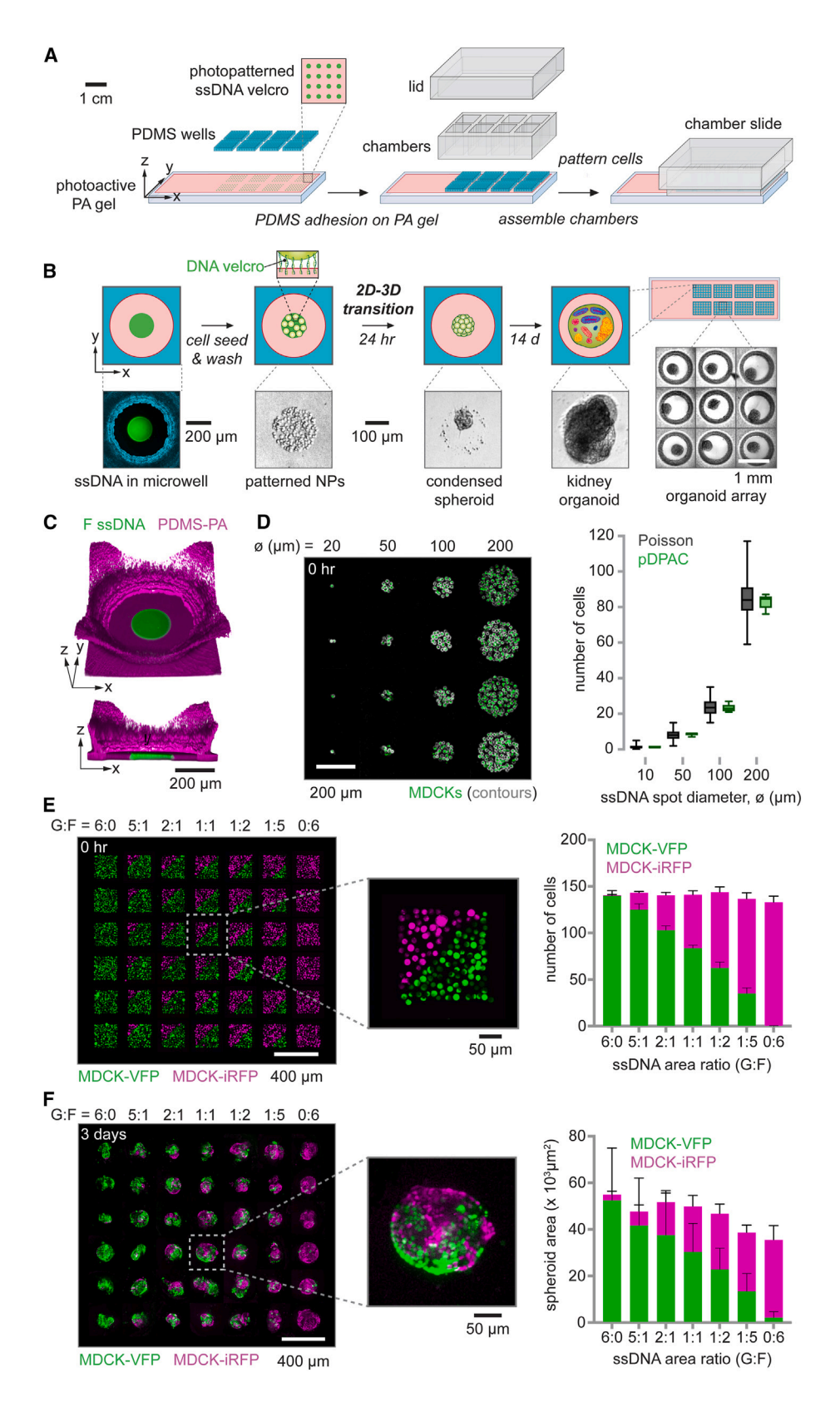
<sup>&</sup>lt;sup>6</sup>Materials Research Science and Engineering Center (MRSEC), University of Pennsylvania, Philadelphia, PA 19104, USA

<sup>&</sup>lt;sup>7</sup>Institute for Regenerative Medicine, University of Pennsylvania, Philadelphia, PA 19104, USA

<sup>&</sup>lt;sup>8</sup>Lead contact

<sup>\*</sup>Correspondence: ajhughes@seas.upenn.edu https://doi.org/10.1016/j.cels.2024.06.004





(legend on next page)



of organoids and other pluripotent cell cultures can bias their development toward specific outcomes. 34-36 Emerging efforts for kidney organoids have begun to demonstrate similar advantages, for example, by miniaturizing kidney organoid production 11,33 or standardizing geometric features using bioprinting. However, scalable suspension culture methods lack control over initial cell quantities, imparting variability in microorganoids, 5,11 whereas microwell systems rely on geometric confinement to produce single organoids per well. 37,38 Thus, no engineering approach has combined precise control of initial size and cell composition (independent of physical boundary conditions), extended culture/imaging, and high throughput.

Here, we modulate organoid outcomes by adjusting the numbers and ratios of kidney progenitors seeded into organoid cultures. We integrate a high-precision, rapid cell patterning technology-photolithographic DNA-programmed assembly of cells (pDPAC)<sup>39-44</sup>—with a microwell organoid culture system. With pDPAC, we can spatially pattern kidney progenitor cell types in defined numbers and ratios at the onset of tissue culture. Furthermore, implementing pDPAC in a 3D microwell array allows us to set the position and physical boundary conditions on developing organoids. This enables unencumbered expansion of cultures over time in a format suited to long-term tracking of individual organoid development. With the precision afforded by our method, we demonstrate that minor adjustments in initial cell composition alter organoid outcomes, as they bias between different organoid morphologies over time. This rectifies a source of variation in previous organoid protocols that did not precisely control initial cell composition. In our organoids differentiated from hiPSC-derived nephron progenitors (NPs), we observed an increase in proximal tubule and a decrease in distal tubule proportions with increasing organoid size, as controlled by the initial numbers of NPs patterned using pDPAC. In mosaic organoids, distal tubule proportion and organoid endpoint size increased with increasing initial NP:UB tip cell ratio, while proximal tubule proportion peaked at a 1:1 ratio. Our work makes advances that will benefit organoid models of disease, screens, and next-generation tissue assembly strategies for producing replacement renal tissues.

#### **RESULTS**

To decouple organoid size from boundary constraints, we adapted a precise and rapid cell patterning technology,

pDPAC, 39-44 to a microwell format suited to long-term organoid culture (Figures 1A and 1B). We targeted three design opportunities: (1) precise hiPSC-derived progenitor cell number and compositional control, (2) transition of 2D patterns to self-organized 3D spheroids open to continued differentiation, and (3) sequestering individual organoids in optically accessible microwells through 15+-day culture periods, enabling imaging and preventing aggregation (Figures 1A, 1B, and S1). A key advance was to follow transient 2D cell patterning on the culture substrate with a transition to 3D culture/differentiation. We achieve 2D patterning via single-stranded DNA (ssDNA) photolithographically bound with high spatial precision to a photoactive polyacrylamide (PPA) substrate on a glass slide; ssDNA spot diameters in the range of 10-200  $\mu$ m were within 22%  $\pm$  25% of their nominal diameters on the corresponding photolithography mask and within 5% coefficient of variation (CV) for a given diameter (Figure S2). We incorporate complementary lipid-conjugated ssDNAs into cell membranes by passive insertion such that they are transiently displayed on cell membranes. 41,43 Base-pairing between cell- and PPA substrate-bound ssDNAs thereby creates temporary adhesions for cell patterning. Multiple orthogonal ssDNA sequences can be serially patterned for multiplexing cell populations.

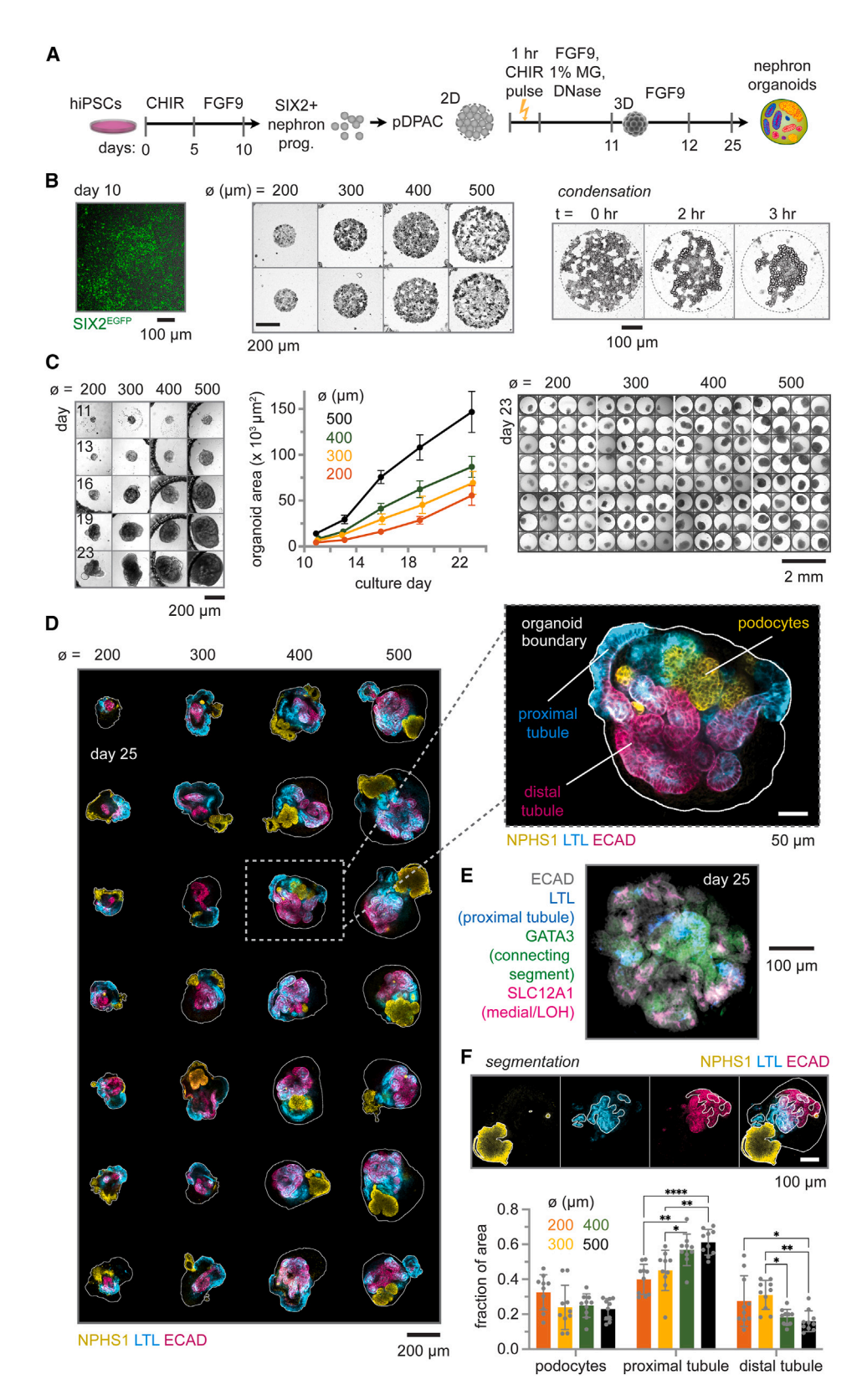
In order to sequester 3D cultures long-term, we integrated microwells with our system. To create microwell walls, sheets of conical polydimethylsiloxane (PDMS) through-hole arrays were fabricated by replica micromolding. These were passivated with a polyacrylamide (PA) brush layer and registered and adhered to DNA micropatterns to within 15.7  $\pm$  10.3  $\mu$ m (mean  $\pm$  SD, n = 16 patterns within microwells) (Figures 1C and S3; Video S1; STAR Methods). Each array was positioned to be compatible with a removable 4 × 2 culture chamber overlay, which divided each slide into 8 independent culture chambers (Figure 1A). During preliminary validation, we found that microwell arrays did not interfere with Madin-Darby canine kidney (MDCK) cell patterning, retained low non-specific cell adhesion properties, and minimized subsequent spheroid spreading/migration (Figure S4; STAR Methods). pDPAC increased precision in patterned cell number for a 200  $\mu m$  spot size from 11% to 4.5% CV relative to that predicted by Poisson loading (Figure 1D). After patterning, MDCKs formed 3D spheroids spontaneously within ∼6 h, with 2% Matrigel increasing aggregation efficiency. Confocal imaging and growth curves showed that spheroid size was predicted by ssDNA

## Figure 1. Overview of integrated cell patterning and microwell system, with validation of long-term compositional modulation via precise control over initial cell number and ratio

(A) Schematic of polyacrylamide (PA) gel cell patterning substrate, photopatterned with adhesive ssDNA, and non-adhesive PDMS microwell overlays and their assembly in standard chamber slide format for 8-plex microwell cultures.

- (B) Schematic of assay for example of hiPSC-derived SIX2+ NP lineage patterning and differentiation to nephron organoids.
- (C) 3D rendering of example ssDNA feature and associated microwell, with rhodamine-methacrylamide co-monomer incorporated into the non-adhesive PA coating for visualization.
- (D) Left, montage of fluorescence micrographs of representative MDCK cell patterns over a range in ssDNA spot sizes. The montage is a composite with the bright-field channel processed with "find edges" in FIJI to emphasize cell contours. Right, box and whisker plot of patterned cell numbers by spot diameter ( $n \ge 9$  spots per condition), along with Poisson distribution expected for passive microwell seeding, modeled using  $\lambda$  = mean of experiment distribution and n = 200 random Poisson-distributed numbers.
- (E) Montage of representative micrographs of MDCK cell patterning on dual ssDNA patterns and corresponding cell number histogram (mean  $\pm$  SD, n = 10 patterns per area ratio).
- (F) Left, sum slices projection micrograph montage of representative condensed 3D mosaic spheroids created from the 2D MDCK cell patterns in (E) after 72 h in culture. Right, histogram of sum of histone H2B-fluorescent protein (FP) marker areas in 10  $\mu$ m step confocal planes over the range of ssDNA patterning area ratios (mean  $\pm$  SD,  $n \ge 6$  patterns per area ratio).





(legend on next page)



pattern diameter 1-3 days after the transition to 3D culture (Figures S4B and S4C). When orthogonal ssDNA strands were used to pattern independent MDCK populations, cell number ratio was modulated in a manner dependent upon pattern area ratio, and differences in spheroid composition were retained 72 h after the 3D transition (Figures 1E, 1F, and S5; Video S2). We verified that using multiple unique ssDNA strands to pattern ratios of the two MDCK populations in juxtaposition ("multiplexed") gave an advantage in precision over patterning of premixed cells at different ratios using a single ssDNA ("mixed"; Figure S6). We counted MDCK-VFP and MDCK-iRFP cells prior to mixing them in a 1:1 ratio and patterning them on 200  $\times$  200  $\mu m$  square patterns of a single ssDNA. Although we achieved comparable median cell ratios, we found that variance was 8× higher in the mixed group and 7× higher in a model of Poisson-distributed loading relative to the multiplexed group. Together, these data validated precise 2D cell patterning on ssDNA and a transition into 3D spheroids of controlled size and composition that persisted after extended culture.

We next tackled kidney organoid culture, starting first with the production of nephron organoids from varying initial quantities of hiPSC-derived NPs. We differentiated SIX2+ NPs<sup>15,45</sup> (Figures 2A and 2B) lacking mature lineage marker expression prior to patterning (Figure S7). Patterning NPs in microwells using pDPAC, we triggered a 2D-to-3D transition by cleaving ssDNA tethers using DNase and then continued differentiation. Cells successfully condensed into single organoids within  $\sim\!4$  h (Figure 2B; Video S3) in the presence of 1% Matrigel. 233 of 240 wells (97%) contained single organoids, and only 3 (1.3%) were empty at the differentiation endpoint. By contrast, after 6 days, cells that had been passively seeded by gravity typically formed multiple rather than single organoids in a cell-densitydependent manner (Figure S8). This validates that NPs aggregate with nearby neighbors, which can be decoupled from persistent geometric constraint and accomplished by achieving close cell-cell proximity on ssDNA islands.

To determine if the initial cell number could be used to gain control over organoid size and cell composition, we patterned NPs on ssDNA features with diameters ø of 200–500  $\mu m$ . After 15 days of differentiation, projected organoid area faithfully reflected differences in initial pattern diameter (Figure 2C). We wondered if the starting pattern size would also change differentiation outcomes. Organoids expressed markers for podocytes (NPHS1/nephrin), proximal tubule (LTL), medial/loop of Henle (SLC12A1), distal tubule (ECAD+ LTL-), and connecting segment (GATA3) nephron cell types (Figures 2D and 2E) and surrounding stromal-like cells (MEIS1/2/3, Figure S9) at the endpoint. Our culture system was compatible with varying protocols, e.g., shortening differentiation

from 10 to 7 days before pDPAC and applying a CHIR pulse (Figure 2E), which tends to distalize organoids. 19 Additionally, it was compatible with NPs derived from a different cell line, PENN123i-SV20 hiPSCs<sup>46</sup> (Figure S10). We segmented day 25 immunofluorescence z stacks and quantified cross-sectional areas for podocytes, proximal tubule, and distal tubule (Figures 2F and S11). The starting pattern size impacted organoid composition. In particular, the representation of proximal tubule as a % of all non-stromal structures significantly increased from 40% ± 8.6% to 61%  $\pm$  7.3% from pattern size ø of 200–500  $\mu m$ (mean  $\pm$  SD, n = 10 organoids per ø). We observed similar trends in nephron segmentation in a replicate experiment in which we supplemented medium with 10 ng mL<sup>-1</sup> recombinant human laminin-521 instead of 1% Matrigel during the lifting and aggregation phase of the NPs (Figure S12). Thus, micropatterning control of the initial NP number offers control over organoid size, which affects cell differentiation.

Our data thus far suggested that pDPAC was compatible with 2D patterning, 3D aggregation, and differentiation of the NP lineage toward multiple kidney cell types. We next recognized an opportunity to leverage the multiplexed patterning capabilities of pDPAC to produce mosaic organoids by co-patterning both hiPSC-derived NPs and UB tip cells (Figure 3A), mimicking their juxtaposition in vivo.47 We focused on these two cell types because reciprocal regulation of NP and UB cell populations through non-autonomous cues appears to be crucial to setting kidney size and nephron endowment during kidney morphogenesis.48-51 UB tip cells were trans-differentiated from distal nephron cells<sup>15</sup> (Figure S13A), forming ruffled epithelial organoids with appropriate expression of GATA3, RET (Figure 3B), and additional markers (ECAD, cytokeratin) consistent with UB identity<sup>15</sup> (Figure S13B). We conducted a viability assay after patterning UB tip cells on ssDNA spots with diameters ø 500  $\mu$ m (Figure S13C). Among patterned cells, 99.2%  $\pm$  0.4% were viable post pDPAC (mean  $\pm$  SD, n = 5 patterns of UB tip cells. STAR Methods). We then created mosaic organoids ranging in initial ssDNA area ratios (1:5, 1:2, 1:1, 2:1, 5:1), directing independent adhesion of NPs and UB tip cells to a constant 300 µm square pattern (Figure 3C). Patterned cell ratios differed from nominal ssDNA area ratios by only 11.0%  $\pm$  5.2% (mean  $\pm$ SD,  $n \ge 4$  patterns per ratio) (Figure S14). Mosaic NP/UB tip cell patterns created with pDPAC successfully condensed into 3D spheroids within 24-48 h after DNase treatment (Figure 3C). Next, we scanned culture parameters to find suitable induction/culture conditions for mosaic NP/UB organoids (STAR Methods). When NPs were exposed to a 60 min, 7 µM CHIR pulse prior to pDPAC, NP and UB populations sorted, forming "core-shell" morphologies mimicking the in vivo interface

Figure 2. Initial NP number biases the emergence of cell types along the early nephron proximal-distal axis (A) Patterning and differentiation timeline.

<sup>(</sup>B) Left, immunofluorescence of SIX2<sup>EGFP</sup> progenitors prior to pDPAC. Middle, montage of bright-field examples after cell patterning for ssDNA feature diameters ø. Images were processed with find edges in FIJI to emphasize cell contours. Right, frames from Video S3 showing 2D to 3D transition.

<sup>(</sup>C) Left, time points of representative organoids formed from 2D patterns of different  $\emptyset$ . Middle, representative growth curves (mean  $\pm$  SD, n = 10 organoids per group). Right, organoid montage at day 23 time point.

<sup>(</sup>D) Representative confocal immunofluorescence sections of organoids at day 25 endpoint. Organoids were manually segmented and arranged as a montage on a black background for clarity. Inset, detail of organoid and cell lineages.

<sup>(</sup>E) Similar organoid from cells differentiated for 7 rather than 10 days in monolayer prior to patterning. LOH, loop of Henle.

<sup>(</sup>F) Top, segmentation scheme for cell types in day 25 organoids. Bottom, plot of organoid composition (ratio of cell type area to total area of all cell types measured, mean  $\pm$  SD, 3–7 slices per n = 10 organoids per  $\phi$ , Tukey's multiple comparisons test, \*p  $\leq$  0.05, \*\*p  $\leq$  0.01, \*\*\*p  $\leq$  0.001, \*\*\*p  $\leq$  0.001).

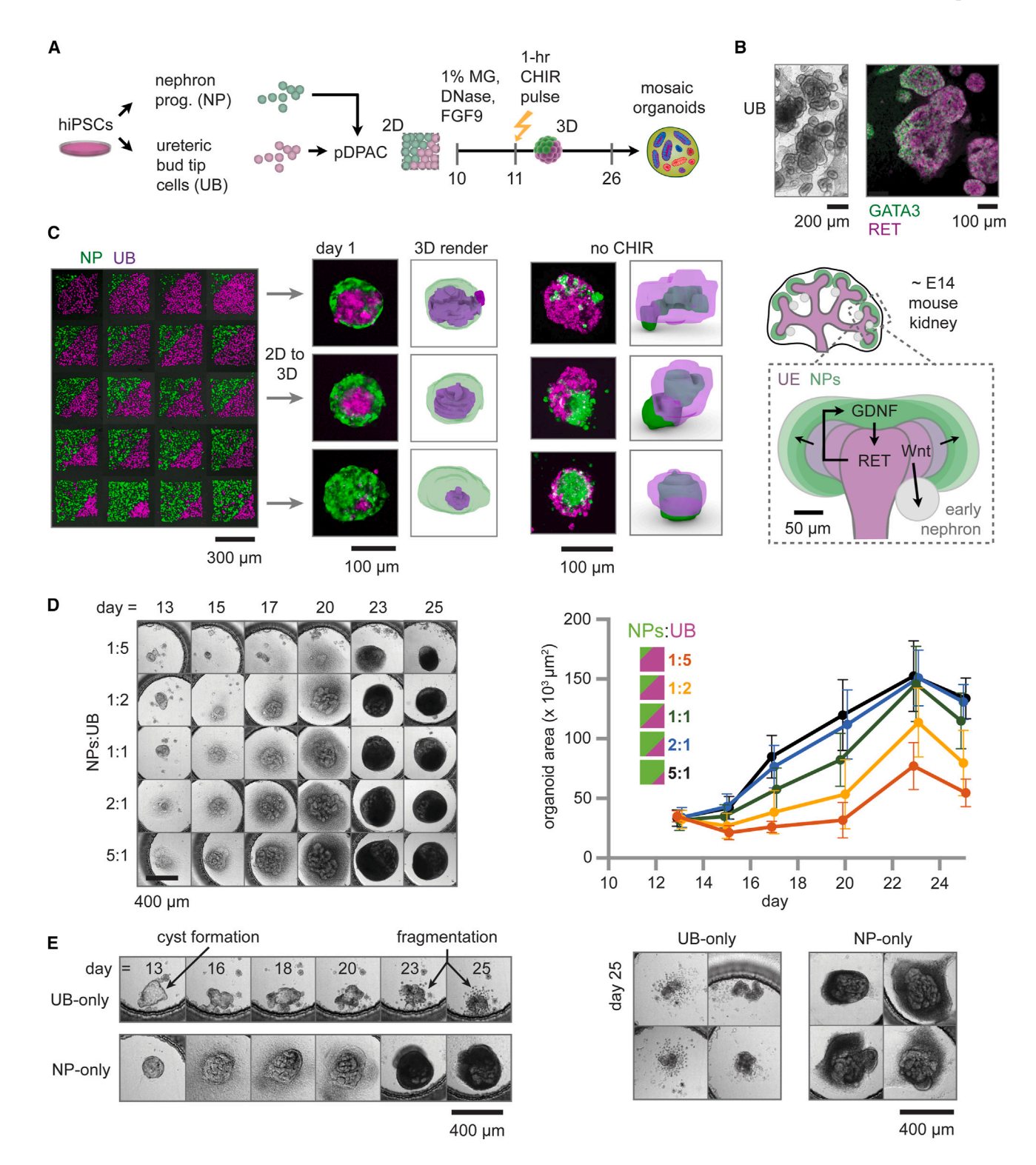


Figure 3. NP/UB tip cell mosaic organoids model the nephrogenic niche interface and grow in a ratio-dependent manner

(A) Patterning and differentiation timeline.

- (B) Confocal micrographs of GATA3+ RET+ UB tip cell organoids.
- (C) Montage of representative fluorescently labeled UB tip cell and NP co-patterns and transition to 3D culture ± NP CHIR pulse prior to patterning. Right, schematic of *in vivo* niche geometry and signaling (UE, ureteric epithelium).
- (D) Left, time point images of example mosaic organoids formed from 2D patterns of different NP:UB tip cell ratios. Right, representative growth curves (mean  $\pm$  SD,  $n \ge 6$  organoids per group).
- (E) Example NP-only and UB tip cell-only organoid controls (left) over time and (right) at culture day 25.



(Figure 3C) and the self-organization of dissociated mouse embryonic kidney cells. <sup>52,53</sup> However, without the CHIR pulse, sorting was inverted, and NPs formed cores (Figure 3C). A shift in NP cadherin expression via canonical WNT signaling could explain the change in cell sorting outcome as dictated by differential adhesion. <sup>54–56</sup> Our data demonstrate successful integration of distinct hiPSC-derived progenitor lineages into mosaic organoids after cell patterning.

We next sought to understand the long-term influence of initial cell ratio on organoid morphology and composition. We started by tracking the growth of mosaic organoids, collecting bright-field images every 2–3 days throughout culture in microwells. Mosaic organoid growth increased with increasing NP:UB tip cell ratio, implying higher proliferation of NPs relative to UB (Figure 3D). NP-only control organoids grew steadily compared with UB-only controls, which formed cystic structures that inflated, deflated, and fragmented (Figure 3E). Substrate-adherent, stromal-like cells were found in mosaic NP/UB tip cell organoids and NP-only controls but not in UB-only controls (Figure 3E). Regardless of starting ratio, mosaic organoids displayed a phase of reducing area between days 23 and 25 post cell patterning, likely due to tissue compaction. These data demonstrate the effect of starting kidney progenitor ratio on organoid growth and long-term viability.

To analyze the effects of NP:UB tip cell ratio on endpoint composition, we performed confocal immunofluorescence analysis of day 26 mosaic and control organoids (Figure 4). We used markers of ureteric epithelium (UE)/connecting segment (GATA3+ ECAD+), calbindin 1+ tissue (CALB1+), distal tubule (ECAD+ LTL- GATA3-), proximal tubule (LTL+), and podocytes (NPHS1+). Through manual image segmentation, we found that only 1 of 10 organoids derived from an initial NP:UB tip cell patterning ratio of 1:5 produced NP-derived proximal tubule, distal tubule, or podocytes (Figures 4C and S15). Moving to a 1:2 initial NP:UB tip cell ratio rescued nephron structure formation in 9 of 10 organoids, suggesting that a minimum number or ratio of NPs is required for nephrogenesis. The proportion of proximal tubule structures increased and then decreased with increasing initial NP cell ratio (Figures 4C and S15B), peaking at 1:1. This suggests a "goldilocks" NP:UB tip cell ratio that maximizes proximal tubule. Since no such peak was found in NP-only organoids, this indicates an interaction between NP cell-autonomous and nonautonomous cues from the UB or UB-derived cells in proximal tubule induction. 19,58 Distal tubule monotonically increased with increasing initial NP:UB tip cell ratio, while GATA3+ ECAD+ connecting segment/UE structures decreased (Figures 4C and \$15B). Together, these data show that modulating the initial ratio of NPs:UB tip cells in mosaic organoids shifts the representation of epithelial tissue types along the proximal-distal axis.

We saw no significant differences in the proportion of CALB1+ structures and only minor differences in representation of podocytes across all starting ratios (Figure S15). Although not specific to UE *in vivo*, CALB1 is highly upregulated there throughout development. <sup>15,30,59,60</sup> In developing human embryonic kidneys, specificity of CALB1 to UE has been shown to extend through gestational week 28. <sup>60,61</sup> Furthermore, in previous hiPSC-derived mosaic NP/UB organoids, CALB1+ structures were derived exclusively from UB tip cells and not from SIX2+ NPs. <sup>60</sup> Therefore, it is highly likely that CALB1+ structures in our mosaic organoids are also UB-derived. In rare instances (3/50 organoids), we

observed complete *in vivo*-like connection of CALB1+ structures with GATA3+ ECAD+ connecting segment/UE, along with proper distal-to-proximal segmentation. We observed an equivalent number of CALB1+ structures juxtaposed but not contiguous with GATA3+ ECAD+ structures (Figure 4D). In controls, CALB1+ structures were not observed, implying that NP and UB interaction is required for CALB1 upregulation. Overall, our results demonstrate emergent inductive phenomena in mosaic NP/UB tip cell organoids. These include changes in cell state of presumptive UB-derived tissues and some connectivity/juxtaposition of these tissues to distal nephron structures.

The interaction of NPs and UB tip cells also altered the organization and volume of mature epithelialized structures and stromal-like populations. Tight conglomerates of multiple tubules with proximal or distal identities formed in NP-only organoids. However, in mosaic organoids, individual tubules were separated by stromal-like cells and were often spatially aligned, either radially or laterally (Figure S16A). We quantified the interdigitation of stromal-like cells between epithelialized structures in mosaic and NP-only organoids. To size-match the final organoid area for comparison, we selected NP-only organoids originally patterned on 500  $\mu m$  ssDNA spots and mosaic organoids with a nominal 2:1 NP:UB tip cell patterning ratio. We then manually segmented the epithelialized structures in the approximate midplane of each organoid. We calculated the organoid solidity, defined as the collective area of the epithelialized structures divided by the area of their convex hull (Figure S16). We found that NP-only organoids had a solidity of  $0.88 \pm 0.06$ , whereas mosaic organoid solidity was lower at 0.62  $\pm$  0.07 (mean  $\pm$  SD, n = 10 organoids for each condition). This result indicates higher separation of individual epithelial structures by interdigitating stromal-like cells in mosaic organoids. Moreover, in some ratios of mosaic organoids that were provided fewer NPs than NP-only organoids, areas of nephron structures were larger. For example, organoids differentiated from NPs patterned on ssDNA spots with an area of 7.07  $\times$  $10^4 \text{ um}^2$  ( $\phi = 300 \text{ um}$ ) had  $6.90 \times 10^4 \pm 2.36 \times 10^4 \text{ um}^2$  (mean  $\pm$ SD, n = 10 organoids) of nephron structures, whereas mosaic organoids with NP:UB tip cell ratio of 1:1 patterned on a smaller ssDNA area of 4.50  $\times$  10<sup>4</sup>  $\mu$ m<sup>2</sup> had higher areas of these nephron structures, totaling  $8.75 \times 10^4 \pm 2.57 \times 10^4 \,\mu\text{m}^2$  (Figure S17A). This result implies expansion of the cap mesenchyme population and/or higher proliferation of committed NP progeny<sup>62</sup> in mosaic organoids where UB cells are present. Expansion of the stromallike population was even higher in mosaic organoids compared with NP-only organoids (Figure S17B). The stromal-like population comprised 55.6%  $\pm$  9.2% (mean  $\pm$  SD, n = 40, 10 organoids per Ø) of the segmented areas of the NP-only organoids, whereas it comprised  $80.9\% \pm 5.3\%$  (mean  $\pm$  SD, n = 50, 10 organoids per ratio) in mosaic NP/UB tip cell organoids. In both cases, stroma increased proportionally with overall organoid size such that there were no significant differences in stromal proportions across all NP-only or mosaic organoid conditions, although we observed a minor decreasing trend in NP-only organoids (Figure \$17C). Our data suggest that inductive cell-cell interactions in mosaic NP/UB tip cell organoids synergistically increase organoid growth, predominantly in a stromal compartment that interdigitates between epithelial structures.

Taken together, these data show that initial NP:UB tip cell ratio in mosaic kidney organoids modulates compositional outcomes



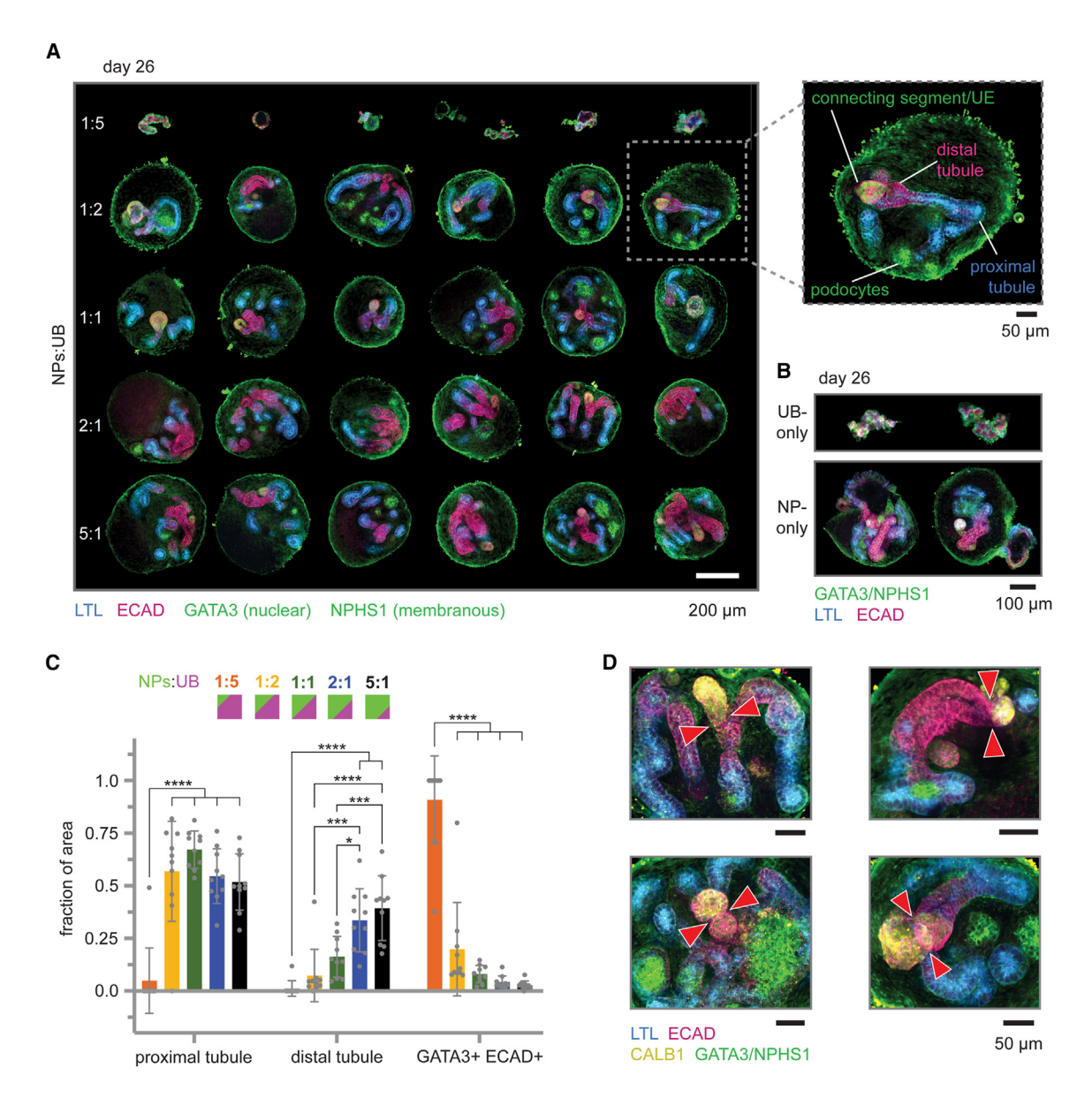


Figure 4. NP/UB tip cell mosaic organoids trigger cell ratio-dependent emergent patterning

(A) Representative confocal immunofluorescence sections of organoids at day 26 endpoint. Organoids were manually segmented and arranged as a montage on a black background for clarity.

- (B) Example endpoint UB-only and NP-only controls, immunostained, segmented, and montaged as in (A).
- (C) Mosaic organoid composition (ratio of cell type area to total area of all cell types measured) vs. NP:UB tip cell pattern area ratios (mean  $\pm$  SD, 1–8 slices per n = 10 organoids per ratio, Tukey's multiple comparisons test, \* $p \le 0.05$ , \*\* $p \le 0.01$ , \*\*\*\* $p \le 0.001$ , \*\*\*\* $p \le 0.0001$ ).
- (D) Example calbindin+ (CALB1+) structures, with rare connections to (3/50 organoids) or juxtaposition to (3/50 organoids) distal nephron structures. Arrowheads denote connected (top) and unconnected (bottom) junctions.

through emergent inductive phenomena. Adjusting epithelial progenitor ratios shifts the representation of total nephron tissue, cell types along the proximal-distal axis, and epithelial vs. stromal tissues, while enabling some higher-order connectivity between UB and NP-derived structures.

#### **DISCUSSION**

Our modified pDPAC system integrates precision cell patterning with microwells for long-term 3D culture. We observed various

trends in emergent organoid morphology and composition based on initial progenitor patterning parameters. In NP-derived organoids, we first found positive correlations between progenitor number, organoid size, and the relative representation of proximal tubule tissue after differentiation. Meanwhile, in mosaic NP/UB tip cell organoids, we observed positive correlations between NP:UB tip cell ratio, final organoid size, and proportion of distal tubule. We also observed a goldilocks 1:1 NP:UB tip cell ratio that optimized formation of proximal tubule structures, as well as a distinctive separation and alignment of individual



epithelialized structures in mosaic vs. NP-only organoids. These data may be consistent with a recent study that suggests proximal tubule cell identity is favored in organoids that undergo extended mesodermal patterning prior to nephrogenesis. 19 To demonstrate this, Vanslambrouck et al. prolonged the culture of differentiating NPs in monolayer under exposure to exogenous WNT agonist CHIR, NOTCH inhibitor DAPT, and BMP7, expanding the SIX2+ metanephric population. In turn, this NP population more frequently contributed to proximal rather than distal tubules in nephron organoids. Here in our mosaic organoids, cues provided to NPs by UB tip cells may have similarly maintained and expanded the metanephric population prior to nephrogenesis. This resulted in the highest proximal tubule proportion at the 1:1 NP:UB tip cell ratio, which was countered by an increase in distal tubule proportion with increasing NP:UB tip cell ratio. However, further investigation is needed to fully understand the underlying mechanism of these results.

In other organoid models, high homogeneity is possible when starting from controlled aggregates of a single progenitor cell type, such as in the formation of gut organoids from Lgr5+ stem cells.<sup>63</sup> However, formation of the kidney in vivo requires non-autonomous interactions between several progenitor populations (UB tip cells, NPs, and interstitial/stromal progenitors) with separate developmental origins.<sup>28-30</sup> This likely explains the failure of kidney organoids to recreate all early kidney cell types in the same protocol. 19,29,64 The field has therefore turned to co-culture models that combine several progenitors, 3,15,17,18 which formed our rationale to tightly control progenitor number and composition in our work with mosaic organoids. The balance between proliferation and differentiation within NPs in the cap mesenchyme is tightly dependent on reciprocal cues exchanged with nearby UB tips. 49,50 For example, Cebrian et al. genetically ablated a fraction of GDNF-expressing cap mesenchyme cells in mouse embryonic kidneys and found a self-correcting mechanism in which the branching rate of UB epithelium reduced to maintain a constant proportion of cap mesenchyme cells to UE tips. 48 In our in vitro cultures of mosaic organoids, we did not observe UB branching or high proliferation of UB tip cells upon co-culture with NPs, in keeping with previous work. 15 Rather, the higher expansion of nephron structures that occurred in the presence of UB tip cells indicates that at least part of the self-correction effect in vivo may operate through a mechanism of NP and/or committed NP progeny proliferation independent of a feedback through UB branching rate.

Although we successfully modulated the morphogenetic and compositional outcomes of the nephrogenic niche, our inability to do the same for the UB compartment—as well as a lack of efficient presumptive connectivity between these two niches—suggests several areas for future development. Ongoing studies to pinpoint differences in cell diversity and maturity between organoids and fetal kidneys may outline additional cell intrinsic or microenvironmental factors that must be added to guided differentiation approaches. Similarly, improved directed differentiation efforts may finally create the full complement of progenitors needed to reconstitute the kidney, in particular, human kidney stromal cell lineages. Exerting engineering control in the timing and spatial assembly of different progenitors may improve the potential for kidney organoids to achieve long-range organiza-

tion beyond that accessible by self-organization. For instance, in future work, we will leverage the multiplexing capabilities and custom patterning of pDPAC to assay more complex initial 2D cell geometries that, once transitioned to 3D, adopt more physiologically inspired tissue shapes and spatial organization. These could include 2D configurations that result in 3D branched or elongated morphologies, predictably break symmetry, and/or precisely adjust the quantity and relative positions of different cell compartments within organoids. Concurrently, new synthetic biology approaches, such as reporter iPSC lines and optogenetic control of cell biophysical or signaling properties, for may be useful to monitor and drive a higher diversity of collective cell dynamics that functionally integrate tissue populations.

We have advanced precision cell patterning for 3D organoid culture to improve throughput, imaging accessibility, and size homogeneity while offering new capabilities for control over morphogenetic outcome. Our work expands upon cell aggregation by centrifugation, agitation, or seeding in microwells, 2,4,11,33,63 which lack precise control over organoid size and composition, and cell patterning in 2D that lacks a transition to 3D self-organization.<sup>34</sup> We contribute an integrated ssDNA-based cell patterning and long-term microwell culture platform that is compatible with hiPSC-derived cell lineages. Our technology offers opportunities for automation and tracking that enable studies of growth, cell sorting, segmentation, and fusion of different structures/cell populations. These advances enable controlled initial conditions and downstream screens applicable to diverse organoid and synthetic embryo systems.

#### **STAR**\***METHODS**

Detailed methods are provided in the online version of this paper and include the following:

- KEY RESOURCES TABLE
- RESOURCE AVAILABILITY
  - Lead contact
  - Materials availability
  - Data and code availability
- EXPERIMENTAL MODEL AND SUBJECT DETAILS
  - Cell lines
  - hiPSC-derived NPs
  - o hiPSC-derived UB tip cells
- METHOD DETAILS
  - Gels for single-stranded DNA photopatterning
  - Photomasks for ssDNA patterning
  - o Patterning of ssDNA on PA gels for pDPAC
  - o PDMS microwell fabrication
  - o PDMS microwell passivation
  - o PDMS microwell adhesion to PA gels
  - o Cell patterning in microwells
  - Cell viability assay
  - O Device assembly and culture
  - Immunofluorescence
  - Imaging
  - Image analysis
  - Adhesion and alignment of PDMS through-hole overlays on PA base gels patterned with ssDNA
  - o Reducing nonspecific cell adhesion in microwells
  - Exogenous canonical WNT activation in mosaic NP/UB tip cell organoids and conditions that improve cell viability
- QUANTIFICATION AND STATISTICAL ANALYSIS





#### SUPPLEMENTAL INFORMATION

Supplemental information can be found online at https://doi.org/10.1016/j.cels.2024.06.004.

#### **ACKNOWLEDGMENTS**

We thank Louis Prahl for advice on DNA patterning conditions, Ananya Gupta and Wenli Yang for advice on hiPSC maintenance, Sarah Howden and Melissa Little for advice on hiPSC differentiation protocols, and Magdalena Niewiadomska-Bugaj for advice on statistical analyses. This research was conducted in part at the Singh Center for Nanotechnology at the University of Pennsylvania, which is supported by the NSF National Nanotechnology Coordinated Infrastructure Program under grant NNCI-2025608. This work was supported by an NSF GRFP award (C.M.P.), NIH NIGMS MIRA R35GM13380 (A.J.H.), and an NSF CAREER award 2047271 (A.J.H.) and was partially supported through the University of Pennsylvania Materials Research Science and Engineering Center (NSF MRSEC, DMR-2309043).

#### **AUTHOR CONTRIBUTIONS**

C.M.P. conceived of and developed technology, designed and conducted experiments, collected and analyzed data, prepared the manuscript, and secured funding. G.C.Q. analyzed data and revised the manuscript. S.H.G. maintained cell cultures and revised the manuscript. A.J.H. conceived of technology, analyzed data, prepared the manuscript, supervised the research, and secured funding.

#### **DECLARATION OF INTERESTS**

The authors declare no competing interests.

Received: November 14, 2023 Revised: April 9, 2024 Accepted: June 17, 2024 Published: July 8, 2024

#### REFERENCES

- McMahon, A.P. (2016). Development of the mammalian kidney. Curr. Top. Dev. Biol. 117, 31–64. https://doi.org/10.1016/bs.ctdb.2015.10.010.
- Czerniecki, S.M., Cruz, N.M., Harder, J.L., Menon, R., Annis, J., Otto, E.A., Gulieva, R.E., Islas, L.V., Kim, Y.K., Tran, L.M., et al. (2018). Highthroughput screening enhances kidney organoid differentiation from human pluripotent stem cells and enables automated multidimensional phenotyping. Cell Stem Cell 22, 929–940.e4. https://doi.org/10.1016/j.stem. 2018.04.022.
- Taguchi, A., and Nishinakamura, R. (2017). Higher-order kidney organogenesis from pluripotent stem cells. Cell Stem Cell 21, 730–746.e6. https://doi.org/10.1016/j.stem.2017.10.011.
- Takasato, M., Er, P.X., Chiu, H.S., Maier, B., Baillie, G.J., Ferguson, C., Parton, R.G., Wolvetang, E.J., Roost, M.S., Chuva de Sousa Lopes, S.M., et al. (2015). Kidney organoids from human iPS cells contain multiple lineages and model human nephrogenesis. Nature 526, 564–568. https:// doi.org/10.1038/nature15695.
- Przepiorski, A., Sander, V., Tran, T., Hollywood, J.A., Sorrenson, B., Shih, J.-H., Wolvetang, E.J., McMahon, A.P., Holm, T.M., and Davidson, A.J. (2018). A simple bioreactor-based method to generate kidney organoids from pluripotent stem cells. Stem Cell Rep. 11, 470–484. https://doi.org/ 10.1016/j.stemcr.2018.06.018.
- Lawlor, K.T., Vanslambrouck, J.M., Higgins, J.W., Chambon, A., Bishard, K., Arndt, D., Er, P.X., Wilson, S.B., Howden, S.E., Tan, K.S., et al. (2021).
   Cellular extrusion bioprinting improves kidney organoid reproducibility and conformation. Nat. Mater. 20, 260–271. https://doi.org/10.1038/ s41563-020-00853-9.

- Jager, K.J., Kovesdy, C., Langham, R., Rosenberg, M., Jha, V., and Zoccali, C. (2019). A single number for advocacy and communicationworldwide more than 850 million individuals have kidney diseases. Kidney Int. 96, 1048–1050. https://doi.org/10.1016/j.kint.2019.07.012.
- Al-Awqati, Q., and Oliver, J.A. (2002). Stem cells in the kidney. Kidney Int. 61, 387–395. https://doi.org/10.1046/j.1523-1755.2002.00164.x.
- van den Berg, C.W., Ritsma, L., Avramut, M.C., Wiersma, L.E., van den Berg, B.M., Leuning, D.G., Lievers, E., Koning, M., Vanslambrouck, J.M., Koster, A.J., et al. (2018). Renal subcapsular transplantation of PSC-derived kidney organoids induces Neo-vasculogenesis and significant glomerular and tubular maturation in vivo. Stem Cell Rep. 10, 751–765. https://doi.org/10.1016/j.stemcr.2018.01.041.
- Morizane, R., Lam, A.Q., Freedman, B.S., Kishi, S., Valerius, M.T., and Bonventre, J.V. (2015). Nephron organoids derived from human pluripotent stem cells model kidney development and injury. Nat. Biotechnol. 33, 1193–1200. https://doi.org/10.1038/nbt.3392.
- Kumar, S.V., Er, P.X., Lawlor, K.T., Motazedian, A., Scurr, M., Ghobrial, I., Combes, A.N., Zappia, L., Oshlack, A., Stanley, E.G., et al. (2019). Kidney micro-organoids in suspension culture as a scalable source of human pluripotent stem cell-derived kidney cells. Development 146, dev172361. https://doi.org/10.1242/dev.172361.
- Garreta, E., Prado, P., Tarantino, C., Oria, R., Fanlo, L., Martí, E., Zalvidea, D., Trepat, X., Roca-Cusachs, P., Gavaldà-Navarro, A., et al. (2019). Fine tuning the extracellular environment accelerates the derivation of kidney organoids from human pluripotent stem cells. Nat. Mater. 18, 397–405. https://doi.org/10.1038/s41563-019-0287-6.
- Mae, S.-I., Ryosaka, M., Sakamoto, S., Matsuse, K., Nozaki, A., Igami, M., Kabai, R., Watanabe, A., and Osafune, K. (2020). Expansion of human iPSC-derived ureteric bud organoids with repeated branching potential. Cell Rep. 32, 107963. https://doi.org/10.1016/j.celrep.2020.107963.
- Mae, S.-I., Ryosaka, M., Toyoda, T., Matsuse, K., Oshima, Y., Tsujimoto, H., Okumura, S., Shibasaki, A., and Osafune, K. (2018). Generation of branching ureteric bud tissues from human pluripotent stem cells. Biochem. Biophys. Res. Commun. 495, 954–961. https://doi.org/10. 1016/j.bbrc.2017.11.105.
- Howden, S.E., Wilson, S.B., Groenewegen, E., Starks, L., Forbes, T.A., Tan, K.S., Vanslambrouck, J.M., Holloway, E.M., Chen, Y.-H., Jain, S., et al. (2021). Plasticity of distal nephron epithelia from human kidney organoids enables the induction of ureteric tip and stalk. Cell Stem Cell 28, 671–684.e6. https://doi.org/10.1016/j.stem.2020.12.001.
- Combes, A.N., Zappia, L., Er, P.X., Oshlack, A., and Little, M.H. (2019).
   Single-cell analysis reveals congruence between kidney organoids and human fetal kidney. Genome Med. 11, 3. https://doi.org/10.1186/ s13073-019-0615-0.
- Zeng, Z., Huang, B., Parvez, R.K., Li, Y., Chen, J., Vonk, A.C., Thornton, M.E., Patel, T., Rutledge, E.A., Kim, A.D., et al. (2021). Generation of patterned kidney organoids that recapitulate the adult kidney collecting duct system from expandable ureteric bud progenitors. Nat. Commun. 12, 3641. https://doi.org/10.1038/s41467-021-23911-5.
- Tanigawa, S., Tanaka, E., Miike, K., Ohmori, T., Inoue, D., Cai, C.-L., Taguchi, A., Kobayashi, A., and Nishinakamura, R. (2022). Generation of the organotypic kidney structure by integrating pluripotent stem cellderived renal stroma. Nat. Commun. 13, 611. https://doi.org/10.1038/ s41467-022-28226-7.
- Vanslambrouck, J.M., Wilson, S.B., Tan, K.S., Groenewegen, E., Rudraraju, R., Neil, J., Lawlor, K.T., Mah, S., Scurr, M., Howden, S.E., et al. (2022). Enhanced metanephric specification to functional proximal tubule enables toxicity screening and infectious disease modelling in kidney organoids. Nat. Commun. 13, 5943. https://doi.org/10.1038/s41467-022-33623-z.
- Shi, M., McCracken, K.W., Patel, A.B., Zhang, W., Ester, L., Valerius, M.T., and Bonventre, J.V. (2023). Human ureteric bud organoids recapitulate branching morphogenesis and differentiate into functional collecting duct cell types. Nat. Biotechnol. 41, 252–261. https://doi.org/10.1038/ s41587-022-01429-5.

## **Cell Systems**

#### Report



- Little, M.H., and Combes, A.N. (2019). Kidney organoids: accurate models or fortunate accidents. Genes Dev. 33, 1319–1345. https://doi.org/10. 1101/gad.329573.119.
- Nishinakamura, R. (2023). Advances and challenges toward developing kidney organoids for clinical applications. Cell Stem Cell 30, 1017–1027. https://doi.org/10.1016/j.stem.2023.07.011.
- Romero-Guevara, R., Ioannides, A., and Xinaris, C. (2020). Kidney organoids as disease models: strengths, weaknesses and perspectives. Front. Physiol. 11, 563981. https://doi.org/10.3389/fphys.2020.563981.
- Phipson, B., Er, P.X., Combes, A.N., Forbes, T.A., Howden, S.E., Zappia, L., Yen, H.-J., Lawlor, K.T., Hale, L.J., Sun, J., et al. (2019). Evaluation of variability in human kidney organoids. Nat. Methods 16, 79–87. https:// doi.org/10.1038/s41592-018-0253-2.
- Subramanian, A., Sidhom, E.-H., Emani, M., Vernon, K., Sahakian, N., Zhou, Y., Kost-Alimova, M., Slyper, M., Waldman, J., Dionne, D., et al. (2019). Single cell census of human kidney organoids shows reproducibility and diminished off-target cells after transplantation. Nat. Commun. 10, 5462. https://doi.org/10.1038/s41467-019-13382-0.
- Wu, H., Uchimura, K., Donnelly, E.L., Kirita, Y., Morris, S.A., and Humphreys, B.D. (2018). Comparative analysis and refinement of human PSC-derived kidney organoid differentiation with single-cell transcriptomics. Cell Stem Cell 23, 869–881.e8. https://doi.org/10.1016/j.stem.2018.
- Wu, H., and Humphreys, B.D. (2020). Single cell sequencing and kidney organoids generated from pluripotent stem cells. Clin. J. Am. Soc. Nephrol. 15, 550–556. https://doi.org/10.2215/CJN.07470619.
- Kobayashi, A., Valerius, M.T., Mugford, J.W., Carroll, T.J., Self, M., Oliver, G., and McMahon, A.P. (2008). Six2 defines and regulates a multipotent self-renewing nephron progenitor population throughout mammalian kidney development. Cell Stem Cell 3, 169–181. https://doi.org/10.1016/j. stem.2008.05.020.
- Taguchi, A., Kaku, Y., Ohmori, T., Sharmin, S., Ogawa, M., Sasaki, H., and Nishinakamura, R. (2014). Redefining the in vivo origin of metanephric nephron progenitors enables generation of complex kidney structures from pluripotent stem cells. Cell Stem Cell 14, 53–67. https://doi.org/10. 1016/j.stem.2013.11.010.
- Lindström, N.O., Guo, J., Kim, A.D., Tran, T., Guo, Q., De Sena Brandine, G., Ransick, A., Parvez, R.K., Thornton, M.E., Baskin, L., et al. (2018). Conserved and divergent features of mesenchymal progenitor cell types within the cortical nephrogenic niche of the human and mouse kidney. J. Am. Soc. Nephrol. 29, 806–824. https://doi.org/10.1681/ASN. 2017080800
- Sato, T., Vries, R.G., Snippert, H.J., van de Wetering, M., Barker, N., Stange, D.E., van Es, J.H., Abo, A., Kujala, P., Peters, P.J., et al. (2009).
   Single Lgr5 stem cells build crypt-villus structures in vitro without a mesenchymal niche. Nature 459, 262–265. https://doi.org/10.1038/nature07935.
- Homan, K.A., Gupta, N., Kroll, K.T., Kolesky, D.B., Skylar-Scott, M., Miyoshi, T., Mau, D., Valerius, M.T., Ferrante, T., Bonventre, J.V., et al. (2019). Flow-enhanced vascularization and maturation of kidney organoids in vitro. Nat. Methods 16, 255–262. https://doi.org/10.1038/s41592-019-0325-y.
- Tran, T., Song, C.J., Nguyen, T., Cheng, S.-Y., McMahon, J.A., Yang, R., Guo, Q., Der, B., Lindström, N.O., Lin, D.C.-H., et al. (2022). A scalable organoid model of human autosomal dominant polycystic kidney disease for disease mechanism and drug discovery. Cell Stem Cell 29, 1083–1101.e7. https://doi.org/10.1016/j.stem.2022.06.005.
- Warmflash, A., Sorre, B., Etoc, F., Siggia, E.D., and Brivanlou, A.H. (2014).
   A method to recapitulate early embryonic spatial patterning in human embryonic stem cells. Nat. Methods 11, 847–854. https://doi.org/10.1038/nmeth.3016.
- Bauwens, C.L., Peerani, R., Niebruegge, S., Woodhouse, K.A., Kumacheva, E., Husain, M., and Zandstra, P.W. (2008). Control of human embryonic stem cell colony and aggregate size heterogeneity influences differentiation trajectories. Stem Cells 26, 2300–2310. https://doi.org/10. 1634/stemcells.2008-0183.

- Lancaster, M.A., Corsini, N.S., Wolfinger, S., Gustafson, E.H., Phillips, A.W., Burkard, T.R., Otani, T., Livesey, F.J., and Knoblich, J.A. (2017). Guided self-organization and cortical plate formation in human brain organoids. Nat. Biotechnol. 35, 659–666. https://doi.org/10.1038/nbt.3906.
- Thomsen, A.R., Aldrian, C., Bronsert, P., Thomann, Y., Nanko, N., Melin, N., Rücker, G., Follo, M., Grosu, A.L., Niedermann, G., et al. (2017). A deep conical agarose microwell array for adhesion independent three-dimensional cell culture and dynamic volume measurement. Lab Chip 18, 179–189. https://doi.org/10.1039/c7lc00832e.
- Stevens, K.R., Ungrin, M.D., Schwartz, R.E., Ng, S., Carvalho, B., Christine, K.S., Chaturvedi, R.R., Li, C.Y., Zandstra, P.W., Chen, C.S., et al. (2013). InVERT molding for scalable control of tissue microarchitecture. Nat. Commun. 4, 1847. https://doi.org/10.1038/ncomms2853.
- Selden, N.S., Todhunter, M.E., Jee, N.Y., Liu, J.S., Broaders, K.E., and Gartner, Z.J. (2012). Chemically programmed cell adhesion with membrane-anchored oligonucleotides. J. Am. Chem. Soc. *134*, 765–768. https://doi.org/10.1021/ja2080949.
- Weber, R.J., Liang, S.I., Selden, N.S., Desai, T.A., and Gartner, Z.J. (2014). Efficient targeting of fatty-acid modified oligonucleotides to live cell membranes through step-wise assembly. Biomacromolecules 15, 4621–4626. https://doi.org/10.1021/bm501467h.
- Todhunter, M.E., Jee, N.Y., Hughes, A.J., Coyle, M.C., Cerchiari, A., Farlow, J., Garbe, J.C., LaBarge, M.A., Desai, T.A., and Gartner, Z.J. (2015). Programmed synthesis of three-dimensional tissues. Nat. Methods 12, 975–981. https://doi.org/10.1038/nmeth.3553.
- Gartner, Z.J., and Bertozzi, C.R. (2009). Programmed assembly of 3-dimensional microtissues with defined cellular connectivity. Proc. Natl. Acad. Sci. USA 106, 4606–4610. https://doi.org/10.1073/pnas. 0900717106.
- Viola, J.M., Porter, C.M., Gupta, A., Alibekova, M., Prahl, L.S., and Hughes, A.J. (2020). Guiding cell network assembly using shape-morphing hydrogels. Adv. Mater. 361, 2002195.
- Prahl, L.S., Porter, C.M., Liu, J., Viola, J.M., and Hughes, A.J. (2023). Independent control over cell patterning and adhesion on hydrogel substrates for tissue interface mechanobiology. iScience 26, 106657. https://doi.org/10.1016/j.isci.2023.106657.
- Vanslambrouck, J.M., Wilson, S.B., Tan, K.S., Soo, J.Y.-C., Scurr, M., Spijker, H.S., Starks, L.T., Neilson, A., Cui, X., Jain, S., et al. (2019). A toolbox to characterize human induced pluripotent stem cell-derived kidney cell types and organoids. J. Am. Soc. Nephrol. 30, 1811–1823. https:// doi.org/10.1681/ASN.2019030303.
- Pashos, E.E., Park, Y., Wang, X., Raghavan, A., Yang, W., Abbey, D., Peters, D.T., Arbelaez, J., Hernandez, M., Kuperwasser, N., et al. (2017). Large, diverse population cohorts of hiPSCs and derived hepatocyte-like cells reveal functional genetic variation at blood lipid-associated loci. Cell Stem Cell 20, 558–570.e10. https://doi.org/10.1016/j.stem. 2017.03.017.
- Short, K.M., Combes, A.N., Lefevre, J., Ju, A.L., Georgas, K.M., Lamberton, T., Cairncross, O., Rumballe, B.A., McMahon, A.P., Hamilton, N.A., et al. (2014). Global quantification of tissue dynamics in the developing mouse kidney. Dev. Cell 29, 188–202. https://doi.org/10. 1016/j.devcel.2014.02.017.
- Cebrian, C., Asai, N., D'Agati, V., and Costantini, F. (2014). The number of fetal nephron progenitor cells limits ureteric branching and adult nephron endowment. Cell Rep. 7, 127–137. https://doi.org/10.1016/j.celrep.2014. 02.033.
- Costantini, F., and Kopan, R. (2010). Patterning a complex organ: branching morphogenesis and nephron segmentation in kidney development.
   Dev. Cell 18, 698–712. https://doi.org/10.1016/j.devcel.2010.04.008.
- Little, M.H., and McMahon, A.P. (2012). Mammalian kidney development: principles, progress, and projections. Cold Spring Harb. Perspect. Biol. 4, a008300. https://doi.org/10.1101/cshperspect.a008300.
- Perl, A.J., Schuh, M.P., and Kopan, R. (2022). Regulation of nephron progenitor cell lifespan and nephron endowment. Nat. Rev. Nephrol. 18, 683–695. https://doi.org/10.1038/s41581-022-00620-w.





- Lefevre, J.G., Chiu, H.S., Combes, A.N., Vanslambrouck, J.M., Ju, A., Hamilton, N.A., and Little, M.H. (2017). Self-organisation after embryonic kidney dissociation is driven via selective adhesion of ureteric epithelial cells. Development 144, 1087–1096. https://doi.org/10.1242/dev.140228.
- Unbekandt, M., and Davies, J.A. (2010). Dissociation of embryonic kidneys followed by reaggregation allows the formation of renal tissues. Kidney Int. 77, 407–416. https://doi.org/10.1038/ki.2009.482.
- Combes, A.N., Davies, J.A., and Little, M.H. (2015). Cell-cell interactions driving kidney morphogenesis. Curr. Top. Dev. Biol. 112, 467–508. https://doi.org/10.1016/bs.ctdb.2014.12.002.
- 55. Steinberg, M.S. (1963). Reconstruction of tissues by dissociated cells. Some morphogenetic tissue movements and the sorting out of embryonic cells may have a common explanation. Science 141, 401–408. https://doi.org/10.1126/science.141.3579.401.
- Bao, M., Cornwall-Scoones, J., Sanchez-Vasquez, E., Cox, A.L., Chen, D.-Y., De Jonghe, J., Shadkhoo, S., Hollfelder, F., Thomson, M., Glover, D.M., et al. (2022). Stem cell-derived synthetic embryos self-assemble by exploiting cadherin codes and cortical tension. Nat. Cell Biol. 24, 1341–1349. https://doi.org/10.1038/s41556-022-00984-y.
- Turlier, H., and Maître, J.-L. (2015). Mechanics of tissue compaction.
   Semin. Cell Dev. Biol. 47–48, 110–117. https://doi.org/10.1016/j.semodb 2015 08 001
- Lindström, N.O., Lawrence, M.L., Burn, S.F., Johansson, J.A., Bakker, E.R.M., Ridgway, R.A., Chang, C.-H., Karolak, M.J., Oxburgh, L., Headon, D.J., et al. (2015). Integrated β-catenin, BMP, PTEN, and Notch signalling patterns the nephron. eLife 3, e04000. https://doi.org/10.7554/ eLife.04000.
- Georgas, K., Rumballe, B., Wilkinson, L., Chiu, H.S., Lesieur, E., Gilbert, T., and Little, M.H. (2008). Use of dual section mRNA in situ hybridisation/ immunohistochemistry to clarify gene expression patterns during the early stages of nephron development in the embryo and in the mature nephron of the adult mouse kidney. Histochem. Cell Biol. 130, 927–942. https://doi. org/10.1007/s00418-008-0454-3.
- Tsujimoto, H., Kasahara, T., Sueta, S.-I., Araoka, T., Sakamoto, S., Okada, C., Mae, S.-I., Nakajima, T., Okamoto, N., Taura, D., et al. (2020). A modular differentiation system maps multiple human kidney lineages from pluripotent stem cells. Cell Rep. 31, 107476. https://doi.org/10. 1016/j.celrep.2020.03.040.
- Lindström, N.O., McMahon, J.A., Guo, J., Tran, T., Guo, Q., Rutledge, E., Parvez, R.K., Saribekyan, G., Schuler, R.E., Liao, C., et al. (2018). Conserved and divergent features of human and mouse kidney organogenesis. J. Am. Soc. Nephrol. 29, 785–805. https://doi.org/10.1681/ ASN.2017080887.
- Georgas, K., Rumballe, B., Valerius, M.T., Chiu, H.S., Thiagarajan, R.D., Lesieur, E., Aronow, B.J., Brunskill, E.W., Combes, A.N., Tang, D., et al. (2009). Analysis of early nephron patterning reveals a role for distal RV proliferation in fusion to the ureteric tip via a cap mesenchyme-derived connecting segment. Dev. Biol. 332, 273–286. https://doi.org/10.1016/j.ydbio.2009.05.578.
- Brandenberg, N., Hoehnel, S., Kuttler, F., Homicsko, K., Ceroni, C., Ringel, T., Gjorevski, N., Schwank, G., Coukos, G., Turcatti, G., et al. (2020). Highthroughput automated organoid culture via stem-cell aggregation in microcavity arrays. Nat. Biomed. Eng. 4, 863–874. https://doi.org/10.1038/ s41551-020-0565-2.
- Howden, S.E., Vanslambrouck, J.M., Wilson, S.B., Tan, K.S., and Little, M.H. (2019). Reporter-based fate mapping in human kidney organoids confirms nephron lineage relationships and reveals synchronous nephron formation. EMBO Rep. 20, e47483. https://doi.org/10.15252/embr. 201847483.
- Wilson, S.B., and Little, M.H. (2021). The origin and role of the renal stroma.
   Development 148, dev199886. https://doi.org/10.1242/dev.199886.
- Kumar Gupta, A., Sarkar, P., Wertheim, J.A., Pan, X., Carroll, T.J., and Oxburgh, L. (2020). Asynchronous mixing of kidney progenitor cells potentiates nephrogenesis in organoids. Commun. Biol. 3, 231. https://doi.org/ 10.1038/s42003-020-0948-7.

- Toda, S., Blauch, L.R., Tang, S.K.Y., Morsut, L., and Lim, W.A. (2018).
   Programming self-organizing multicellular structures with synthetic cell-cell signaling. Science 361, 156–162. https://doi.org/10.1126/science.aat0271.
- Toda, S., McKeithan, W.L., Hakkinen, T.J., Lopez, P., Klein, O.D., and Lim, W.A. (2020). Engineering synthetic morphogen systems that can program multicellular patterning. Science 370, 327–331. https://doi.org/10.1126/ science.abc0033.
- Hughes, A.J., and Herr, A.E. (2012). Microfluidic Western blotting. Proc. Natl. Acad. Sci. USA 109, 21450–21455. https://doi.org/10.1073/pnas. 1207754110
- Schindelin, J., Arganda-Carreras, I., Frise, E., Kaynig, V., Longair, M., Pietzsch, T., Preibisch, S., Rueden, C., Saalfeld, S., Schmid, B., et al. (2012). Fiji: an open-source platform for biological-image analysis. Nat. Methods 9, 676–682. https://doi.org/10.1038/nmeth.2019.
- Schmid, B., Schindelin, J., Cardona, A., Longair, M., and Heisenberg, M. (2010). A high-level 3D visualization API for Java and ImageJ. BMC Bioinformatics 11, 274. https://doi.org/10.1186/1471-2105-11-274.
- Hughes, A.J., and Herr, A.E. (2010). Quantitative enzyme activity determination with zeptomole sensitivity by microfluidic gradient-gel zymography. Anal. Chem. 82, 3803–3811. https://doi.org/10.1021/ac100201z.
- Kang, J.H., Um, E., and Park, J.-K. (2009). Fabrication of a poly(dimethylsiloxane) membrane with well-defined through-holes for three-dimensional microfluidic networks. J. Micromech. Microeng. 19, 045027. https://doi.org/10.1088/0960-1317/19/4/045027.
- Keskin, D., Mokabbar, T., Pei, Y., and Van Rijn, P. (2018). The relationship between bulk silicone and benzophenone-initiated hydrogel coating properties. Polymers 10, 534. https://doi.org/10.3390/polym10050534.
- Beh, C.W., Zhou, W., and Wang, T.-H. (2012). PDMS-glass bonding using grafted polymeric adhesive–alternative process flow for compatibility with patterned biological molecules. Lab Chip 12, 4120–4127. https://doi.org/ 10.1039/c2lc40315c.
- Schneider, M.H., Willaime, H., Tran, Y., Rezgui, F., and Tabeling, P. (2010).
   Wettability patterning by UV-initiated graft polymerization of poly(acrylic acid) in closed microfluidic systems of complex geometry. Anal. Chem. 82, 8848–8855. https://doi.org/10.1021/ac101345m.
- Ebara, M., Hoffman, J.M., Stayton, P.S., and Hoffman, A.S. (2007).
   Surface modification of microfluidic channels by UV-mediated graft polymerization of non-fouling and 'smart' polymers. Radiat. Phys. Chem. Oxf. Engl. 76, 1409–1413. https://doi.org/10.1016/j.radphyschem.2007.02.072.
- McGinnis, C.S., Patterson, D.M., Winkler, J., Conrad, D.N., Hein, M.Y., Srivastava, V., Hu, J.L., Murrow, L.M., Weissman, J.S., Werb, Z., et al. (2019). MULTI-seq: sample multiplexing for single-cell RNA sequencing using lipid-tagged indices. Nat. Methods 16, 619–626. https://doi.org/ 10.1038/s41592-019-0433-8.
- Prahl, L.S., Viola, J.M., Liu, J., and Hughes, A.J. (2021). The developing kidney actively negotiates geometric packing conflicts to avoid defects. Preprint at bioRxiv. https://doi.org/10.1101/2021.11.29.470441.
- Combes, A.N., Short, K.M., Lefevre, J., Hamilton, N.A., Little, M.H., and Smyth, I.M. (2014). An integrated pipeline for the multidimensional analysis of branching morphogenesis. Nat. Protoc. 9, 2859–2879. https://doi.org/ 10.1038/nprot.2014.193.
- O'Brien, L.L., Combes, A.N., Short, K.M., Lindström, N.O., Whitney, P.H., Cullen-McEwen, L.A., Ju, A., Abdelhalim, A., Michos, O., Bertram, J.F., et al. (2018). Wnt11 directs nephron progenitor polarity and motile behavior ultimately determining nephron endowment. eLife 7, e40392. https://doi.org/10.7554/eLife.40392.
- Patyukova, E., Rottreau, T., Evans, R., Topham, P.D., and Greenall, M.J. (2018). Hydrogen bonding aggregation in acrylamide: theory and experiment. Macromolecules 51, 7032–7043. https://doi.org/10.1021/acs.macromol.8b01118.



- Raos, G., and Zappone, B. (2021). Polymer adhesion: seeking new solutions for an old problem. Macromolecules 54, 10617–10644. https://doi.org/10.1021/acs.macromol.1c01182.
- Karni, M., Zidon, D., Polak, P., Zalevsky, Z., and Shefi, O. (2013). Thermal degradation of DNA. DNA Cell Biol. 32, 298–301. https://doi.org/10.1089/ dna.2013.2056.
- Klapperich, C.M. (2009). Microfluidic diagnostics: time for industry standards. Expert Rev. Med. Devices 6, 211–213. https://doi.org/10.1586/ erd.09.11.
- Naujok, O., Lentes, J., Diekmann, U., Davenport, C., and Lenzen, S. (2014). Cytotoxicity and activation of the Wnt/beta-catenin pathway in mouse embryonic stem cells treated with four GSK3 inhibitors. BMC Res. Notes 7, 273. https://doi.org/10.1186/1756-0500-7-273.
- Bretland, A.J., Lawry, J., and Sharrard, R.M. (2001). A study of death by anoikis in cultured epithelial cells. Cell Prolif. 34, 199–210. https://doi. org/10.1046/j.1365-2184.2001.00198.x.

- Watanabe, K., Ueno, M., Kamiya, D., Nishiyama, A., Matsumura, M., Wataya, T., Takahashi, J.B., Nishikawa, S., Nishikawa, S.-I., Muguruma, K., et al. (2007). A ROCK inhibitor permits survival of dissociated human embryonic stem cells. Nat. Biotechnol. 25, 681–686. https://doi.org/10. 1038/nbt1310.
- Motomura, K., Okada, N., Morita, H., Hara, M., Tamari, M., Orimo, K., Matsuda, G., Imadome, K.-I., Matsuda, A., Nagamatsu, T., et al. (2017).
   A Rho-associated coiled-coil containing kinases (ROCK) inhibitor, Y-27632, enhances adhesion, viability and differentiation of human term placenta-derived trophoblasts in vitro. PLoS One 12, e0177994. https:// doi.org/10.1371/journal.pone.0177994.
- Kurosawa, H. (2012). Application of Rho-associated protein kinase (ROCK) inhibitor to human pluripotent stem cells. J. Biosci. Bioeng. 114, 577–581. https://doi.org/10.1016/j.jbiosc.2012.07.013.





#### **STAR**\***METHODS**

#### **KEY RESOURCES TABLE**

REAGENT or RESOURCE	SOURCE	IDENTIFIER
Antibodies		
Biotinylated Lotus tetragonolobus lectin (LTL)	Vector Laboratories	Cat#B-1325; RRID: AB_2336558
Goat anti-human GATA3	R&D Systems	Cat#AF2605; RRID: AB_2108571
Mouse anti-human E-cadherin (ECAD)	Biosciences	Cat#610181; RRID: AB_397580
Rabbit anti-human E-cadherin (ECAD)	Cell Signaling Technology	Cat#3195; RRID: AB_2291471
Rabbit anti-human SLC12A1	Abcam	Cat#ab171747; RRID: AB_2802126
Sheep anti-human Nephrin	R&D Systems	Cat#AF4269-SP; RRID: AB_2154851
Rabbit anti-human RET	Cell Signaling Technology	Cat#3223; RRID: AB_2238465
Mouse anti-calbindin D-28K (clone CB-955)	Sigma-Aldrich	Cat#C9848; RRID: AB_476894
Mouse anti-pan-cytokeratin (clone 11)	Sigma-Aldrich	Cat#C2931; RRID: AB_258824
Mouse anti-MEIS1/2/3 antibody (clone 9.2.7)	Active Motif	Cat#39796; RRID: AB_2750570
Donkey anti-rabbit AlexaFluor™ 488	Thermo Fisher Scientific	Cat#A21206; RRID: AB_2535792
Donkey anti-mouse AlexaFluor™ 555	Thermo Fisher Scientific	Cat#A31570; RRID: AB_2536180
Donkey anti-rat AlexaFluor™ Plus 555	Thermo Fisher Scientific	Cat#A48270; RRID: AB_2896336
Donkey anti-goat AlexaFluor <sup>TM</sup> Plus 647	Thermo Fisher Scientific	Cat#A32849; RRID: AB_2762840
Donkey anti-sheep AlexaFluor™ 647	Thermo Fisher Scientific	Cat#A-21448; RRID: AB_2535865
Chemicals, peptides, and recombinant proteins	s	
0.25% Trypsin	Thermo Fisher Scientific	Cat#25300056
Fetal bovine serum	Corning	Cat#35-010-CV
Matrigel® hESC-Qualified Matrix	Corning	Cat#354277
Matrigel® Growth Factor Reduced (GFR) Basement Membrane Matrix	Corning	Cat#354230
mTeSR™ Plus medium	STEMCELL Technologies	Cat#100-0276
Gentle Cell Dissociation Reagent	STEMCELL Technologies	Cat#100-0485
StemPro <sup>™</sup> Accutase <sup>™</sup> Cell Dissociation Reagent	Thermo Fisher Scientific	Cat#A1110501
rhLaminin-521	Thermo Fisher Scientific	Cat#A29249
CHIR99021	R&D Systems	Cat#4423
TeSR™-E6 medium	STEMCELL Technologies	Cat#05946
Recombinant human FGF-9 protein	R&D Systems	Cat#273-F9-025
Heparin sodium salt	Sigma-Aldrich	Cat#H4784
Recombinant human FGF basic/FGF2 (146 aa) GMP protein	R&D Systems	Cat#233-GMP-01M
CTS™ TrypLE™ Select Enzyme	Thermo Fisher Scientific	Cat#A1285901
TTNPB (retinoic acid analogue)	Tocris Bioscience	Cat#0761
Y-27632 dihydrochloride	Tocris Bioscience	Cat#1254
PluriSTEM™ Dispase-II	Sigma-Aldrich	Cat#SCM133
KnockOut™ Serum Replacement	Thermo Fisher Scientific	Cat#10828010
SU-8 2025 photoresist	Kayaku Advanced Materials Inc.	Cat#NC9981681
SU-8 developer solution	Kayaku Advanced Materials Inc.	Cat#NC9901158
Dichlorodimethylsilane	Sigma-Aldrich	Cat#440272
Triton™ X-100	Fisher Scientific	Cat#BP151
3-(Trimethoxysilyl)propyl methacrylate	Sigma-Aldrich	Cat#440159-100ML

(Continued on next page)



Continued		
REAGENT or RESOURCE	SOURCE	IDENTIFIER
Acrylamide/Bis-acrylamide, 30% solution	Sigma-Aldrich	Cat#A3699
N-[3-[(4-benzoylphenyl) formamido]propyl] methacrylamide	PharmAgra custom synthesis; Hughes and Herr <sup>69</sup>	CAS:165391-55-9
Sodium dodecyl sulfate (SDS)	Bio-Rad	Cat#161-0301
Ammonium persulfate (APS)	Sigma-Aldrich	Cat#A3678
Tetramethylethylenediamine (TEMED)	Sigma-Aldrich	Cat#T9281
OPBS (10X), no calcium, no magnesium	Thermo Fisher Scientific	Cat#14200075
CD-26 developer	Singh Center for Nanotechnology; Shipley	N/A
Chromium etchant	Sigma-Aldrich	Cat#651826
MICROPOSIT™ Remover 1165	Singh Center for Nanotechnology; Shipley	N/A
Grey resin	Formlabs	Cat#RS-F2-GPGR-04
Dow SYLGARD™ 184 Silicone	Ellsworth Adhesives	Cat#2065622
Benzophenone	Sigma-Aldrich	Cat#B9300-25G-A
Acrylamide	Fisher Scientific	Cat#BP170-500
UltraPure™ 0.5M EDTA	Thermo Fisher Scientific	Cat#15575-038
TURBO™ DNase (2 U/μL)	Thermo Fisher Scientific	Cat#AM2238
Donkey serum	Sigma-Aldrich	Cat#D9663
DyLight™ 405 Streptavidin	Jackson ImmunoResearch	Cat#016-470-084
Critical commercial assays		
SYBR™ Gold nucleic acid gel stain	Thermo Fisher Scientific	Cat#S11494
CellTracker™ Red dye	Thermo Fisher Scientific	Cat#C34552
CellTracker™ Deep Red dye	Thermo Fisher Scientific	Cat#C34565
CellTracker™ Green CMFDA dye	Thermo Fisher Scientific	Cat#C7025
LIVE/DEAD® Cell Imaging Kit (488/570)	Thermo Fisher Scientific	Cat#R37601
Experimental models: Cell lines		
Canine: MDCK-II cell line	gift from Arjun Raj; MilliporeSigma	Cat#00062107-1VL
Canine: MDCK-II H2B-Venus	Viola et al. <sup>43</sup>	N/A
Canine: MDCK-II H2B-iRFP670	Prahl et al.44	N/A
SIX2 <sup>EGFP</sup> reporter hiPSCs	Murdoch Children's Research Institute/ Washington University Kidney Translational Research Center and Division of Nephrology (parental line CRL-2429 from ATCC); Vanslambrouck et al. <sup>45</sup>	N/A
PENN123i-SV20 hiPSCs	University of Pennsylvania iPSC Core Facility; Pashos et al. <sup>46</sup>	RRID: CVCL_EL23
Oligonucleotides		
Photopatterning oligo: polyT20F: 5'-TTTTTTTTTTTTTTTTTA; GAAGAAGAACGAAGAAGAA-3'	IDT; Prahl et al. <sup>44</sup>	N/A
Photopatterning oligo: polyT20G: 5'-TTTTTTTTTTTTTTTTTA; GCCAGAGAGAGAGAGAG-3'	IDT; Prahl et al. <sup>44</sup>	N/A
Lipid ssDNA: Universal Anchor: 5'-TGGAATTCTCGGGTGCCAA; GGGTAACGATCCAGCTGTCACT- ignoceric-amide-3'	Oligo Factory custom synthesis; Viola et al. 43	N/A
Lipid ssDNA: Universal Co-Anchor: 5'-palmitic-amide-AGTGAC; AGCTGGATCGTTAC-3'	Oligo Factory custom synthesis; Viola et al. <sup>43</sup>	N/A

(Continued on next page)





Continued		
REAGENT or RESOURCE	SOURCE	IDENTIFIER
Cell patterning oligo: F' handle: 5'-CCTTGGCACCCGAGAATT; CCATTTTTTTTTTTTTTTTT TTTTCTTCTTCGTTCTTCT-3'	IDT; Prahl et al. <sup>44</sup>	N/A
Cell patterning oligo: G' handle: 5'-CCTTGGCACCCGAGAAT; TCCATTTTTTTTTTTTTTTTT CTCTCTCTCTCTCTGGCT-3'	IDT; Prahl et al. <sup>44</sup>	N/A
Fluorescent probe oligo: FAM_F': 5'-5(6)-carboxyfluorescein-TT; TCTTCTTCGTTCTTCTTCT-3'	IDT; Prahl et al. <sup>44</sup>	N/A
Fluorescent probe oligo: FAM_G': 5'-5(6)-carboxyfluorescein-CT; CTCTCTCTCTCTGGCT-3'	IDT; Prahl et al. <sup>44</sup>	N/A
Fluorescent probe oligo: Cy5_F': 5'-Cy5-TTTCTTCTTCGTTCTTCTTCT-3'	IDT; Prahl et al. <sup>44</sup>	N/A
Software and algorithms		
Fiji/ImageJ	Schindelin et al. <sup>70</sup>	https://imagej.net/ij/
ImageJ 3D Viewer plugin	Schmid et al. <sup>71</sup>	https://imagej.net/ij/plugins/3d-viewer/
LayoutEditor	juspertor GmBH	https://layouteditor.com/
SOLIDWORKS 3D CAD	SolidWorks Corporation	https://www.solidworks.com/
BEAMER	GenlSys	https://www.genisys-gmbh.com/beamer.html
Prism 10	GraphPad	https://www.graphpad.com/
Rhino 7	Robert McNeel & Associates	https://www.rhino3d.com/
NIS-Elements imaging software	Nikon Instruments Incorporated	https://www.microscope.healthcare.nikon.com/products/software/nis-elements
Excel	Microsoft	https://www.microsoft.com/en-us/ microsoft-365/excel
Other		
4" mechanical grade silicon wafer	Singh Center for Nanotechnology; University Wafer, Inc.	N/A
Digital spin coater with vacuum chuck	INSTRAS Scientific	SCK-300P
Fisherbrand™ Isotemp™ Hot Plate Stirrer	Fisher Scientific	Cat#SP88857200
Mylar mask	CAD/Art Services custom order	N/A
365 nm mounted LED	ThorLabs	M365LP1
Aspheric condenser lens	ThorLabs	ACL7560U
Adjustable lens tube	ThorLabs	SM3V10
Ultrasonic cleaning bath	Thermo Fisher Scientific	Cat#15-337-411
DLW-66+ direct laser writer	Singh Center for Nanotechnology; Heidelberg Instruments	N/A
5"x5"x0.90" chrome-on-quartz photomask, IP3500 photoresist	Singh Center for Nanotechnology	N/A
Portable glovebox	Bel-Art	H50028-2001
UV crosslinker oven	Spectro-UV	XL-1000
8-well cell culture slides	MatTek	Cat#CCS-8
		N/A
Form 3 stereolithography (SLA) resin 3D printer	Formlabs	
0	Formlabs	N/A
printer		
printer Form Wash instrument	Formlabs	N/A
printer Form Wash instrument Form Cure instrument	Formlabs Formlabs	N/A N/A

(Continued on next page)



Continued			
REAGENT or RESOURCE	SOURCE	IDENTIFIER	
470 nm mounted LED	ThorLabs	M470L4	
Collimation adapter	ThorLabs	COP1-A	
Stainless steel probe	Fine Science Tools	10140-04	

#### **RESOURCE AVAILABILITY**

#### **Lead contact**

Further information and requests for resources and reagents should be directed to and will be fulfilled by the lead contact, Alex J. Hughes (ajhughes@seas.upenn.edu).

#### **Materials availability**

This study did not generate new unique reagents.

#### **Data and code availability**

- All data reported in this paper will be shared by the lead contact upon request.
- This paper does not report original code.
- Any additional information required to reanalyze the data reported in this paper is available from the lead contact upon request.

#### **EXPERIMENTAL MODEL AND SUBJECT DETAILS**

#### **Cell lines**

Madin-Darby canine kidney cells (MDCKs, female) expressing H2B-VFP or H2B-iRFP (nuclear green and red fluorescence, respectively) were generated in earlier work by lentiviral transduction and maintained as previously described. Briefly, cells were passaged using 0.25% trypsin (Thermo Fisher Scientific, 25300056) and cultured at  $37^{\circ}$ C and 5% CO<sub>2</sub> in T-175 flasks (Corning) in minimum essential medium (MEM, with Earle's Salts and L-glutamine, Corning, 10-010-CM), 1x pen/strep (100 IU mL<sup>-1</sup> penicillin, and 100  $\mu$ g mL<sup>-1</sup> streptomycin, 100x stock, Invitrogen, 15140122), and 10% fetal bovine serum (Corning, 35-010-CV).

Nephron progenitor (NP) and ureteric bud (UB) tip cells were derived from human hiPSCs similarly to previous reports. 11,15,64 SIX2<sup>EGFP</sup> reporter hiPSCs<sup>45</sup> or PENN123i-SV20 hiPSCs<sup>46</sup> were maintained at 37°C and 5% CO<sub>2</sub> on plates coated with Matrigel (hESC-qualified, Corning, 354277) in mTeSR Plus (STEMCELL Technologies, 100-0276) with 1x pen/strep and passaged every 3-4 days using Gentle Cell Dissociation Reagent (STEMCELL Technologies, 100-0485) for clump passaging, or Accutase (Thermo Fisher Scientific, A1110501) for single-cell passaging. Genomic integrity was confirmed by molecular karyotyping through the Induced Pluripotent Stem Cell Core, Penn Institute for Regenerative Medicine.

PENN123i-SV20 (male) was obtained from the University of Pennsylvania iPSC Core Facility. Distribution of this cell line was supported by U01TR001810 from the NIH. The SIX2<sup>EGFP</sup> reporter hiPSCs (SIX2-T2A-EGFP, male, parental line CRL-2429 from ATCC) were obtained from Murdoch Children's Research Institute/Washington University Kidney Translational Research Center and Division of Nephrology.

#### hiPSC-derived NPs

hiPSCs were lifted and dissociated to single-cell suspension with Accutase at  $37^{\circ}$ C, counted with a hemocytometer and seeded at 65,000 cells per well in a 6-well culture plate coated with rhLaminin-521 (Thermo Fisher Scientific, A29249). The following day, induction of intermediate mesoderm began using 7  $\mu$ M CHIR99021 (R&D Systems, 4423), a WNT agonist, in TeSR-E6 medium (STEMCELL Technologies, 05946) with 1x pen/strep for 5 days. Media was then swapped to 200 ng mL $^{-1}$  FGF9 (R&D Systems, 273-F9-025) and 1  $\mu$ g mL $^{-1}$  heparin (Sigma-Aldrich, H4784) in TeSR-E6 with 1x pen/strep for 5 days to induce NPs. On day 10, cells were dissociated with Accutase at  $37^{\circ}$ C to single-cell suspension, diluted 5x with TeSR-E6, and pelleted at 200 g for 3 min.

#### hiPSC-derived UB tip cells

UB tip cells were trans-differentiated from NP cultures derived similarly to the above, except with two adjustments thought to favor anterior intermediate mesoderm from which the ureteric epithelium derives *in vivo* and/or more distal nephron cell identity. <sup>15</sup> Specifically, the CHIR step was reduced to 3 days, and 200 ng mL<sup>-1</sup> FGF9 was replaced with 600 ng mL<sup>-1</sup> FGF2 (R&D Systems, 233-GMP-01M) for 4 days. Cells were then dissociated with TrypLE (Thermo Fisher Scientific, A1285901) at 37°C to single-cell suspension, diluted 5x with TeSR-E6 containing 1x pen/strep and pelleted at 300 g for 2.5 min. Media was aspirated and cells resuspended as a dense slurry in residual media. 2 μL of this slurry were spotted onto 0.4 μm polyester Transwell membranes in 6-well plates, with 4 spots (organoids) per membrane. Organoids received a CHIR pulse by culturing at the air-liquid interface for 1 hr in the presence of 7 μM CHIR99021 in TeSR-E6 medium with 1x pen/strep in the lower Transwell compartment (1.2 mL well<sup>-1</sup>). Media was





swapped to TeSR-E6 supplemented with 1x pen/strep, 600 ng mL $^{-1}$  FGF2, and 1  $\mu$ g mL $^{-1}$  heparin for 5 days, and then to TeSR-E6 supplemented with 1x pen/strep and 0.1  $\mu$ M TTNPB (a retinoic acid analogue, Tocris Bioscience, 0761) for 13 days.

To begin transdifferentiation, day 20-25 organoids were dissociated with 200  $\mu$ L 1:1 TrypLE:Accutase per organoid, occasionally agitating by gentle vortexing and trituration. The suspension was then diluted 5x with TeSR-E6 medium, pelleted for 3 min at 300 g, and resuspended at 6 x 10<sup>6</sup> cells mL<sup>-1</sup> in 200 ng mL<sup>-1</sup> FGF2, 3  $\mu$ M CHIR99021, 0.1  $\mu$ M TTNPB, 10  $\mu$ M Y-27632 (Tocris Bioscience, 1254), 100 ng mL<sup>-1</sup> GDNF, and 1x pen/strep ('UB medium'). At least 6 x 10<sup>5</sup> cells (in 100 LI media) were then plated per well of a 6-well polyester Transwell plate. 1.2 mL of 1:1 Growth Factor Reduced Matrigel (GFR-Matrigel, Corning, 354230):UB medium were added on top of each Transwell, and 2.3-2.5 mL of UB medium were added to each basolateral compartment. For passaging, Matrigel was first digested using 3 mL of dispase per well (PluriSTEM Dispase-II, 1 mg mL<sup>-1</sup>, Sigma-Aldrich, SCM133) and incubated for 10 min in a 15 mL conical tube at 37°C, vortexing gently at 5 min intervals. 9 mL of TeSR-E6 medium with 1x pen/strep was then added and the mixture was pelleted at 500 g for 5 min. Partially degraded Matrigel was then aspirated off and the pellet subjected to continued dissociation with 2 mL of 1:1 TrypLE:accutase at 37°C for 15-25 min with periodic gentle vortexing. 10 mL of DPBS with 2% FBS was added and cells were pelleted at 500 g for 3 min, followed by resuspension as before and Transwell plating. At least one passage was required to obtain a 99% pure UB population, since UB propagation was favored over off-target cells in UB medium. <sup>15</sup> Freezing medium for cell storage consisted of 10% DMSO, 40% knockout serum replacement (Thermo Fisher Scientific, 10828010) 50% TesR-E6, and 10  $\mu$ M Y-27632.

#### **METHOD DETAILS**

#### **Gels for single-stranded DNA photopatterning**

Photoactivatable polyacrylamide (PPA) gels were fabricated on glass slides as previously described. <sup>43</sup> Briefly, according to manufacturer guidelines, SU-8 2025 photoresist (Kayaku Advanced Materials Inc., NC9981681) was coated at a thickness of 30 μm onto mechanical-grade silicon wafers (University Wafer) using a digital spin coater (INSTRAS Scientific, SCK-300P). The wafer was soft baked on a hotplate (Fisher Scientific, SP88857200) at 65°C for 1 min and 95°C for 4 min. After cooling, a Mylar mask, printed with a double-rail pattern at 20,000 d.p.i. (CAD/Art Services), was laid onto SU-8-coated wafers and exposed for 30s to 365 nm UV light from a mounted LED (ThorLabs M365LP1, ACL7560U, SM3V10) at 10 mW/cm², as measured by a light meter (Thorlabs PM100D, S120VC). The Mylar mask was designed to pattern photoresist rails that would run the 75 mm edges of standard glass slides, creating a 30 μm gap between the slide and the silicon wafer for molding of a PA gel layer. Wafers were baked at 65°C for 1 min and 95°C for 3 min after exposure, allowed to cool to RT, developed in an SU-8 developer solution (Kayaku Advanced Materials Inc., NC9901158), and washed with isopropanol, followed by acetone. 2 mL of hydrophobic dichlorodimethylsilane (DCDMS, Sigma-Aldrich, 440272) were deposited on wafers *in vacuo* for 15 min. Silanized wafers were washed thoroughly with deionized (DI) water and dried under a compressed airstream. Between PPA gel fabrications, silicon wafers were washed with 0.1% Triton X-100 (Fisher Scientific, BP151) in DI water, followed by DI water.

Plain 75 x 25 mm glass microscope slides (Corning, 2947-75X25) were rinsed in 0.1% Triton in DI water to remove surface grease and dried under an airstream. Slides were silanized with 3-(TrimethoxysilyI)propyl methacrylate (Sigma-Aldrich, 440159-100ML) to create a monolayer of methacrylate functional groups according to established protocols. 72 Silanized slides were placed, functionalized-side-down, on patterned silicon wafers and manually aligned with their 75 mm edges against SU-8 rails. PA gel precursor solutions were made out of the following: 7% T (w/v% total acrylamides), made from a 30% T, 2.7% C (w/w% of the cross-linker N,Nmethylenebisacrylamide) stock (Sigma-Aldrich, A3699); 3 mM benzophenone-methacrylamide (N-[3-[(4-benzoylphenyl) formamido] propyl] methacrylamide, BPMAC, PharmAgra) from a 100 mM stock in DMSO, 0.06% SDS (Bio-Rad, 161-0301), 0.06% Triton, 0.06% ammonium persulfate (APS, Sigma-Aldrich, A3678), 0.06% tetramethylethylenediamine (TEMED, Sigma-Aldrich, T9281), 1x DPBS (Ca<sup>2+</sup>/Mg<sup>2+</sup>-free, Thermo Fisher Scientific, 14-200-075), and DI water. Partial precursors were made of acrylamides and DPBS and degassed in vacuo in an ultrasonic bath (Thermo Fisher Scientific, 15-337-411) for 1 min. Detergents SDS and Triton were added, followed by BPMAC, and finally, APS and TEMED catalysts. Using a standard 200 LI pipette,  $\sim$ 150  $\mu$ L of precursor solution were then injected into the gap between the methacrylate-functionalized glass slide and silicon wafer. Precursor spread through the gap for ~30 s, and the slide was slid along the length of the rails to allow any remaining bubbles to escape through its 25 mm ends. Excess precursor was removed using a Kimwipe, ensuring flush contact of the slide with the SU-8 rails. The slide was then left alone for 25 min to allow for additional PA polymerization. Following polymerization, 2 mL of DPBS were pipetted against one 25 mm slide edge; at this side, the slide was carefully levered from wafer using a razor blade, with DPBS wicking beneath the gel to aid release. Fabricated slides were stored in DPBS at 4°C for up to 1 week before single-stranded DNA (ssDNA) was photopatterned.

#### **Photomasks for ssDNA patterning**

CAD files for ssDNA spot and square array patterns were designed in LayoutEditor (juspertor GmbH), then finalized and converted to Heidelberg format files in BEAMER software (GenlSys). Custom 5"x5" photomasks were fabricated in a cleanroom facility: Spot/square arrays were exposed on blank chrome-on-quartz masks using a DWL 66+ laser lithography system (Heidelberg Instruments) to direct write on 0.5 µm thick coatings of IP3500 positive photoresist (Shipley). Masks were developed in CD-26 solvent (Shipley), washed in DI water, and dried under compressed nitrogen gas. Areas of exposed/patterned chromium were removed with chromium etchant (Sigma). Masks were again washed in DI water and dried under compressed nitrogen gas. Then, remaining resist was stripped by submerging masks in MICROPOSIT Remover 1165 (Shipley) for 3 min at 60°C. Masks were rinsed with acetone and isopropanol and air-dried.



#### Patterning of ssDNA on PA gels for pDPAC

Oligos (IDT, 5'-T20-X20-3') were patterned on photoactivatable PA gels attached to glass slides. Two oligos were used: "F," where X20 is 5'-AGAAGAAGAACGAAGAAGAA-3' and "G," where X20 is 5'-AGCCAGAGAGAGAGAGAGAG.3'. In a glove box (Bel-Art, H50028-2001) filled with an atmosphere of medical-grade nitrogen, PPA gels were dried under a nitrogen stream. For each slide, a 400 µL solution of 0.25 mM (for MDCK patterning) or 0.375 mM (for hiPSC-derived cells) oligo in 1x DPBS was degassed, moved into the glove box, and sparged with a nitrogen stream for  $\sim$ 30s. The oligo solution was pipetted onto the patterned chrome side of a photomask, and the slide was laid – gel-side-down – onto the liquid bead of oligo solution; starting at an  $\sim$ 45-degree angle, the slide was carefully lowered from one edge to the other, allowing the oligo solution to wick across the PPA gel without introducing bubbles. After manually aligning the slide above the mask pattern and letting it rest for ~1 min, excess oligo solution was removed with a Kimwipe, immobilizing the slide to the mask. The slide-mask sandwich was removed from the glove box, flipped, and exposed to 254 nm light in a UV oven (Spectrolinker XL-1000 UV Crosslinker, Spectronics Corporation) for 2 min at ~9 mW/cm². After 254 nm UV light exposure, 2 mL of 0.1% SDS in DI water were pipetted against one 25 mm slide edge, and the slide was carefully levered from the mask using a razor blade. To remove unadhered oligo, the slide was then soaked for 10 hr in 15 mL of 0.1% SDS in DPBS in a 15-cm petri dish. Fresh solution was used to rinse once more for 20 min, followed by two 20 min washes in DPBS only to remove SDS. In the case of patterning a second oligo, UV exposure to pattern the first oligo was reduced to 110 s, and the slide was dried under an airstream following wash steps. The alignment fiducial marks of the first oligo (G) were stained with a 0.2 µM solution of a custom, fluorescently-tagged complementary oligo (5'-/56-FAM/CTCTCTCTCTCTCTCTGGCT-3', IDT) in DPBS for 10 min and rinsed in a petri dish of DPBS for 5 min prior to drying and application of the second oligo (F) in nitrogen. Upon removal of the slide-mask sandwich from the glove box, the slide was manually aligned on the second mask pattern to the stained oligo G fiducial marks under a 470 nm blue light using an inverted microscope (Eclipse Ts2-FL, Nikon) (Figure S5B). Following 2 min UV light exposure to pattern F oligo, the slide was again carefully levered from the mask and free F oligo was removed through the previously described washing steps. The slide was stored in fresh DPBS at 4°C and dried under an airstream prior to the attachment of polydimethylsiloxane (PDMS) microwells.

#### **PDMS** microwell fabrication

PDMS sheets patterned with through-holes were molded using 3D-printed pillar arrays. Conical frustum pillar arrays were designed in SOLIDWORKS 3D CAD software such that their positions coincided with the layout of the 8 chambers of cell culture slides (MatTek, CCS-8) as well as ssDNA patterns. The arrays were then printed in grey resin (Formlabs, RS-F2-GPGR-04) by a 3D printer (Formlabs Form 3), at a printing resolution of 25 μm. Pillar arrays were post-processed by rinsing in 100% isopropanol (Form Wash instrument, Formlabs), removing from supports, and drying for at least 1 hr. To reduce bowing of the mold, curing processes of UV exposure and baking were done separately. The mold was exposed to UV in a Form Cure instrument (Formlabs) without heat. It was then placed under a glass slide and 500-g weight (Troemner, 61055S) and baked for 24 hr at 60°C. To remove any residual uncured resin in the mold, which could inhibit PDMS curing, it was soaked in isopropanol for 15+ hr and dried.

PDMS sheets were then molded against 3D printed pillar arrays. A 10:1 base to catalyst solution of PDMS silicone rubber (Sylgard 184, Ellsworth Adhesives, 2065622) prepolymer was thoroughly mixed and degassed in a vacuum chamber. Approximately 3 mL of PDMS prepolymer were poured onto the pillar array. A metal spatula was used to spread and level the prepolymer. The tops of the pillars were blown with a gentle airstream. PDMS was baked at 40°C (Heratherm IMH100 Advanced Microbiological Incubator, Thermo Fisher Scientific, 51028067) for 48 hr. Following curing, the tops of pillar arrays were firmly rubbed to remove any residual PDMS; a microporous cosmetic sponge was soaked in isopropanol and wrung out, then used to wipe the tops of the pillars. PDMS sheets were then demolded and washed in 100% isopropanol for 24 hr and air-dried. Before reuse, pillar arrays were rinsed with 100% isopropanol.

#### **PDMS** microwell passivation

Similar to published methods, <sup>74–77</sup> PA was grafted onto PDMS through-hole sheets to passivate against nonspecific cell and protein adhesion during culture. Dry PDMS sheets were placed on a glass microscope slide. Each sheet was then plasma-treated with a hand-held high frequency generator (Electro-Technic Products, Inc., Model BD 10A) in a raster motion for 30 seconds on each side and submerged for 15 min in a 10% v/v solution of 3-(Trimethoxysilyl)propyl methacrylate in acetone. Sheets were then soaked in a 5% w/v solution of benzophenone (Sigma-Aldrich, B9300-25G-A) in acetone for 15 min. In a nitrogen atmosphere, PDMS sheets were flipped on glass slides to remove excess solution and thoroughly dried under nitrogen. They were placed on a slide, top-side (larger through-hole diameter) up. Approximately 1.5 mL of a degassed and nitrogen-sparged solution of 15% w/v acrylamide monomer (Fisher Scientific, BP170-500) in DI water was pipetted onto PDMS sheets. A quartz slide (Thermo Fisher Scientific, AA42297KG) was laid on the PDMS sheets. The quartz-PDMS-glass sandwich was exposed to 254 nm light in a UV oven for 10 min. PDMS sheets were then washed alternately in 70% ethanol, DI water, and 70% ethanol again for 30 min each, and air-dried.

#### PDMS microwell adhesion to PA gels

The DNA-patterned PA gel was dried under an airstream. The four corners and center of each chamber pattern were stained with a solution of 20x SYBR Gold (Invitrogen, S11494) in DI water for 10 min. To remove non-adhered SYBR, the slide was soaked in a petri dish of DPBS for 10 min and air-dried.

For alignment and attachment of PDMS sheets to the PA base gel, the side of each PDMS sheet, which was not cast directly against the 3D-printed mold (i.e., smaller through-hole diameter side), was plasma-treated for 1.5 min in a raster pattern with a





hand-held high frequency generator. The PDMS sheet was immediately submerged in DI water. The PDMS sheet was transferred, plasma-treated side down, onto the PA gel in the approximate region of a chamber's array of ssDNA patterns. SYBR-stained DNA patterns were illuminated using collimated, 470 nm blue LED light (Thorlabs, COP1-A and M470L4) mounted on a ring stand and visualized through a stereo microscope (Nikon, SMZ800N). Before the water dried, a stainless steel probe (Fine Science Tools, 10140-04) was used to manually align each PDMS through-hole sheet, so that DNA patterns were centered in each microwell. The PDMS sheets immobilized upon complete evaporation of DI water. Once each PDMS sheet had been aligned and adhered, a small piece of aluminum foil was laid on the PPA/PDMS microwell slide, followed by a large glass slide (Corning, 2947-75X50) and a 500-g stainless steel weight. The slide was then baked at 70°C for 16-18 hr to anneal the PDMS to the PA gel.

#### **Cell patterning in microwells**

MDCKs and hiPSC-derived NPs and UB tip cells were patterned on ssDNA features within fabricated PDMS/PPA composite microwells. Prior to cell seeding, each microwell slide was soaked in 3% bovine serum albumin in DPBS for 1 hr, rinsed with two changes of DPBS in a petri dish, and stored in fresh DPBS at 4°C until it was needed for cell seeding. Directly prior to seeding, the gel was soaked in 70% ethanol for 30 min and rinsed with two changes of sterile DPBS.

In some experiments, cells were labeled with CellTracker dyes prior to lifting for cell patterning. Lyophilized CellTracker Red (Thermo Fisher Scientific, C34552), Deep Red (Thermo Fisher Scientific, C34565), and Green CMFDA (Thermo Fisher Scientific, C7025), were each resuspended in DMSO to the manufacturer's recommended concentrations. Each was then diluted to 1  $\mu$ M in serum-free MEM. Adherent cells were incubated in CellTracker medium for 30 min at 37°C. CellTracker medium was then removed and the cells were washed with DPBS.

For MDCK patterning, cells grown to ~80% confluency in T-175 polystyrene culture flasks were washed with DPBS and incubated at 37°C in 0.25% Trypsin-EDTA for ~10 min to lift them. MDCKs were resuspended in culture media and centrifuged at 200 g for 3 min at 4°C. They were then washed twice by resuspending in 10 mL of DPBS and re-pelleted by centrifugation. MDCKs were resuspended in 100 μL of DPBS in 1.5 mL Eppendorf tubes (1 tube per T-175) with 1 mM EDTA (Thermo Fisher Scientific, 15575-038) and labeled with lipid-DNAs (custom syntheses, OligoFactory, Holliston, MA): "universal anchor" (5'-TGGAATTCTCGGGTGCCAAGGGTAACGATCCAGCTGTCACT-C24 lignoceric acid-3'), a lipid-conjugated ssDNA, was added to each Eppendorf tube from a 100 μM stock in DI water to a final concentration of 2.5 μM. Then, lipid-conjugated ssDNA "universal co-anchor" (5'-C16 Palmitic acid-AGTGACAGCTGGATCGTTAC-3') was added to a final concentration of 2.5 μM, followed by 2.5 μM final concentration of "adhesion strand" DNA (5'-CCTTGGCACCCGAGAATTCCA-T19-Y20-3', where Y20 is the reverse complement of the X20 sequence patterned on the pDPAC slide). 40,43,78 Each oligo was added in succession to the 100 μL reaction; an 8 min incubation step under gentle agitation on a vortex set at very low speed (~5 Hz) followed each addition. After adding the series of 3 oligos, cells were washed 3 times in 1 mL of DPBS with 1 mM EDTA by pelleting through centrifugation and aspirating off DPBS. At the end of labeling and washing, 600  $\mu$ L of DPBS with 1 mM EDTA were added to each Eppendorf tube, and cells labeled with the same ssDNAs were combined and placed on ice. Excess DPBS was poured off each ssDNApatterned slide. Using a 200 µL pipette, cell suspension was added dropwise over the microwells, such that it fully covered all DNA patterns. Slides rested in a petri dish on ice for 5 min as cells settled in microwells. Then, each slide was dipped repeatedly into a cold bath of DPBS with 1 mM EDTA to remove unpatterned cells. Cell patterns were intermittently checked on an inverted microscope between washes until unpatterned cells had been fully removed from the microwells. For dual MDCK patterns, the second oligo-labeled cells were then added dropwise to the slide and settled for 5 min, and the wash steps to remove nonspecific cells were repeated.

For hiPSC cell-derived pDPAC, some changes were made to the patterning protocol. First, cells were maintained at RT in TeSR E6 medium with 100  $\mu$ M Y-27632 throughout the oligo functionalization steps.  $2.5 \times 10^7$  NPs were functionalized with 5  $\mu$ M each of universal anchor, co-anchor, and adhesion strand F'. Due to the larger surface area of each UB tip cell,  $2 \times 10^7$  UB tip cells were functionalized with 6  $\mu$ M each of universal anchor, co-anchor, and adhesion strand G'. Following, the 3 cell pellet washes to remove excess oligo as well as cell patterning and post patterning microwell washes were carried out in RT DPBS without EDTA. Each oligo reaction of cells was resuspended in 500 ul of DPBS before patterning. For dual NP/UB pDPAC, UB tip cells remained in the last oligo addition and were only washed 3 times and resuspended once NPs had been patterned and the microwells thoroughly washed of unhybridized cells. UB tip cells were then patterned second, followed by microwell washing.

For sufficient cell patterning, approximately  $1.25 \times 10^7$  cells are needed to create a confluent lawn of cells over the ssDNA patterning interface of our culture device. Although >95% of cells were washed from the slide in the assay designs in this work, these unpatterned cells can be recovered and used for parallel experiments or expanded/cryopreserved, depending on the cell type.

#### **Cell viability assay**

In a validation step, UB tip cells patterned alone on G ssDNA spots with diameters  $\emptyset$  of 500  $\mu$ m underwent a viability assay using a LIVE/DEAD® Cell Imaging Kit (488/570) (Thermo Fisher Scientific, R37601). Because the dead cell indicator BOBO-3 lodide stains exposed DNA, we interpreted fully red cells as dead and spotty extracellular red fluorescence as staining of the ssDNA sequences used for pDPAC.



#### **Device assembly and culture**

After pDPAC, slides were loaded into bases of 8-well cell culture chamber slides (MatTek, CCS-8). Gaskets were removed from the manufacturer's provided glass slides and inserted into the grooves of the polystyrene chambers. The chambers were then aligned over the microwell slides and the chamber bases were clamped in place.

For NP-only organoids, patterned cultures were incubated in a pulse of TeSR-E6 with 1x pen/strep, 7  $\mu$ M CHIR99021, and 10  $\mu$ M Y-27632 for 1 hr and exchanged to TeSR-E6 with 1x pen/strep, 10  $\mu$ M Y-27632, 1% GFR-Matrigel, 200 ng mL<sup>-1</sup> FGF9, and 1  $\mu$ g mL<sup>-1</sup> heparin for  $\sim$  3 hr until cells spread on ssDNA patterns and formed visible cell contacts. 15  $\mu$ L of TURBO DNase (Thermo Fisher Scientific, AM2238) were added to each chamber to cleave ssDNA and initiate aggregate formation. The following day, medium was swapped to TeSR-E6 with 1x pen/strep, 200 ng mL<sup>-1</sup> FGF9, and 1  $\mu$ g mL<sup>-1</sup> heparin. Chamber slides were placed on an orbital shaker at 60 rpm for the rest of the culture period (14 days). Two days after pDPAC, medium was swapped to TeSR-E6 with 1x pen/strep and exchanged every 2 days for 13 days.

For NP/UB tip cell mosaic organoids, patterned cells were incubated in TeSR-E6 with 1x pen/strep, 10  $\mu$ M Y-27632, 1% GFR-Matrigel, 100 ng mL<sup>-1</sup> FGF9, 0.5  $\mu$ g mL<sup>-1</sup> heparin, and 2% FBS. After  $\sim$  3 hr, cells had formed visible cell junctions, at which time 15  $\mu$ L of TURBO DNase were added to each chamber to initiate transition to 3D culture. 24 hr later, cultures received a pulse of TeSR-E6 with 1x pen/strep, 7  $\mu$ M CHIR99021, and 10  $\mu$ M Y-27632 for 1 hr at 37°C. Medium was then swapped to TeSR-E6 with 1x pen/strep, 100 ng mL<sup>-1</sup> FGF9, and 0.5  $\mu$ g mL<sup>-1</sup> heparin for 24 hr. Organoids were then maintained in plain TeSR-E6 with 1x pen/strep on an orbital shaker at 60 rpm for the rest of culture, with medium exchanged every 2 days for 13 days.

#### **Immunofluorescence**

Immunofluorescence staining and imaging was performed as previously described, <sup>79</sup> using protocols adapted from Combes et al. and O'Brien et al. <sup>80,81</sup> Briefly, 15 or 16 days post pDPAC, organoids were fixed in 4% paraformaldehyde in DPBS for 45 min, washed three times for 5 min per wash in DPBS, and blocked for 2 hr at room temperature in PBSTX (DPBS + 0.1% Triton X- 100) containing 5% donkey serum (Sigma-Aldrich, D9663). Following, fixed and blocked organoids were incubated in primary and then secondary antibodies in blocking buffer for at least 24 hr each at 4°C, alternating with 3 washes in PBSTX, with a 30 min wait after the first two PBSTX additions, and a 12 to 24 hr wait after the last PBSTX wash.

Primary antibodies and dilutions included biotinylated LTL (1:300, Vector Laboratories, B-1325, RRID:AB\_2336558), goat anti-human GATA3 (1:20, R&D Systems, AF2605, RRID:AB\_2108571), mouse anti-human E-cadherin (1:300, Biosciences, 610181, RRID:AB\_397580), rabbit anti-human E-cadherin (1:300, Cell Signaling Technology, 3195, RRID:AB\_2291471), rabbit anti-human SLC12A1 (1:300, Abcam, ab171747, RRID:AB\_2802126), sheep anti-human Nephrin (1:40, R&D Systems, AF4269-SP, RRID:AB\_2154851), rabbit anti-human RET (1:200, Cell Signaling Technology, 3223, RRID:AB\_2238465), mouse anti-calbindin D-28K (1:500, clone CB-955, Sigma-Aldrich, C9849, RRID: AB\_476894), mouse anti-pan-cytokeratin (1:200, clone 11, Sigma-Aldrich, C2931, RRID:AB\_258824), and mouse anti-MEIS1/2/3 antibody (1:200, clone 9.2.7, Active Motif, 39796, RRID:AB\_2750570). Secondary antibodies (raised in donkey) were used at 1:200 dilution and included anti-rabbit AlexaFluor 488 (Thermo Fisher Scientific, A21206, RRID: AB\_2535792), anti-mouse AlexaFluor 555 (Thermo Fisher Scientific, A31570, RRID: AB\_2536180), anti-rat AlexaFluor Plus 555 (Thermo Fisher, A48270, RRID: AB\_2896336), anti-goat AlexaFluor Plus 647 (Thermo Fisher Scientific, A32849, RRID: AB\_2762840), and anti-sheep AlexaFluor 647 (Thermo Fisher Scientific, A-21448, RRID: AB\_2535865). Finally, DyLight 405-Streptavidin (Jackson ImmunoResearch, 016-470-084) was used to stain biotinylated LTL.

#### **Imaging**

Imaging was performed using a Nikon Ti2-E microscope equipped with a CSU-W1 spinning disk (Yokogawa), a white light LED, laser illumination (100 mW 405, 488, and 561 nm lasers and a 75 mW 640 nm laser), a Prime 95B back-illuminated sCMOS camera (Photometrics), motorized stage, 4x/0.2 NA, 10x/0.25 NA and 20x/0.5 NA lenses (Nikon), and a stagetop environmental enclosure (OkoLabs).

#### **Image analysis**

For longitudinal analyses, we selected organoids derived from progenitor patterns that displayed high initial ssDNA patterning fidelity and coverage and low nonspecific background cell adhesion. Immunofluorescence marker quantification was performed from 3-7 z-slices per NP-only organoid and 1-8 z-slices per mosaic NP/UB tip cell organoid recovered from confocal fluorescence micrograph stacks, consisting of the approximate mid-plane, and respective planes at -25 and +25  $\mu$ m in z, with additional 25  $\mu$ m increments in z to span the organoid volume. For each slice, regions attributed to each marker category–podocytes (NPHS1, in NP-only organoids), proximal tubule (LTL), and distal tubule (ECAD+ LTL- GATA3-)—were manually segmented in Fiji. In mosaic NP/UB tip cell organoids, UE/connecting segment (ECAD+ GATA3+), Calbindin1+ (CALB1+) structures, and podocytes made up a small overall proportion of the organoid compared to the distal and proximal tubule and tended to form more spherical compartments that spanned fewer slices in z. Thus, for these tissues, the projected area of each discrete compartment was segmented and measured. We defined the remaining area of the organoid as a stromal-like population, which was supported by positive MEIS1/2/3 immunostaining. We then calculated the area fraction of each tissue as the total area of each tissue divided by the total area of all measured, non-stromal-like tissues.

In the case of spheroids made from H2B-VFP and H2B-iRFP MDCKs, cultures were segmented on day 3 post cell patterning. Micrograph stacks spanning the full MDCK spheroid volumes and taken in 10  $\mu$ m step increments in z were montaged in Fiji. The fluorescent channels were then separately thresholded and the total areas of the two MDCK populations were calculated.





Organoid growth was tracked using brightfield confocal images taken at 2-3-day intervals throughout organoid culture in microwells. All organoids selected for growth analysis had lifted from PA substrates and rounded by their culture endpoints. At each analyzed time point, the maximum projected area of each organoid was manually segmented and measured. In cases of fragmented organoids or organoids that failed to condense to a single organoid per microwell, the projected areas of the total tissue per microwell were summed. For substrate-adhered organoids, areas of apparent epithelialized structures that stood out from surrounding flattened cells were manually segmented and measured.

3D renderings of CellTracker-stained mosaic organoids were generated by manual segmentation of z slices from confocal fluorescence stacks to create binary stacks, exporting as.stl surface objects from Fiji using the 3D Viewer plugin, <sup>71</sup> followed by importing and rendering in Rhino 7 3D modeling software (Robert McNeel & Associates).

SI movies were created from timelapse and z-stack confocal micrographs using NIS-Elements imaging software (Nikon instruments Inc.) and edited/annotated in Fiji.

#### Adhesion and alignment of PDMS through-hole overlays on PA base gels patterned with ssDNA

When binding PDMS to a substrate, both the PDMS and substrate are typically oxygen plasma-treated, creating reactive groups on both surfaces that create covalent bonds, <sup>75</sup> which may disrupt ssDNA integrity, necessitating an alternative method. Instead, we plasma treated only the polyacrylamide brush layer grafted on the PDMS surface before adhering it to the ssDNA-patterned PA substrate. Plasma treatment creates reactive amide groups on the brush layer that hydrogen bond with the PA substrate. <sup>82</sup> For alignment, we used DI water for two reasons: 1) it allowed us to float through-hole sheets above the ssDNA patterns (visualized using SYBR Gold staining) and manually align their positions before pressing them into tight contact with the substrate, and 2) we hypothesize that the swelling of the polyacrylamide substrate and brush layer increased interfacial entanglement of the polymer chains, improving adhesion. <sup>83</sup> Once the water had evaporated, the through-hole sheets were immobilized on the polyacrylamide substrate. We then used a thermal bonding process at 70°C to further improve adhesion of the PDMS overlay to the ssDNA-patterned substrate. <sup>75</sup> Thermal annealing did not damage ssDNA patterns, as dry DNA remains stable at temperatures below 130°C (ref. <sup>84</sup>).

#### Reducing nonspecific cell adhesion in microwells

One design challenge was to ensure efficient cell capture on ssDNA within microwells, while discouraging non-specific capture of cells. We found advantages here by using a conical rather than a cylindrical well profile, aiding in wash-out of unpatterned cells. Secondly, we required extremely low cell attachment to the microwell walls in order to prevent initial nonspecific cell adhesion as well as organoid spreading and migration out of microwells over relatively long differentiation times. Despite its biofouling property, PDMS was an attractive material for microwell wall fabrication because it is chemically inert, mechanically stable, biocompatible, inexpensive, and easily moldable. We found that among other passive blocking schemes, grafting a non-adhesive linear polyacrylamide brush layer onto the PDMS surface gave the most favorable nonadhesive properties.

#### Exogenous canonical WNT activation in mosaic NP/UB tip cell organoids and conditions that improve cell viability

We found that applying a 7  $\mu$ M CHIR99021 pulse to NPs prior to lifting cells for pDPAC had detrimental effects on NP patterning efficiency within microwells, as it promoted aggregation of cells in suspension and nonspecific cell adhesion to microwell walls. Supplying the CHIR pulse immediately after pDPAC greatly reduced cell viability, particularly for the fully epithelialized UB tip cells, as CHIR is known to be cytotoxic. <sup>86</sup> We therefore patterned both NPs and UB tip cells and supplied the 1 hr CHIR pulse 24 hr later on a background of FGF9 treatment, during which time the mosaic organoids were condensing. We found that this CHIR pulse was necessary for NP-derived nephron structures to form by day 26. This contrasts with recent results by Howden et al., <sup>15</sup> where the presence of UB tip cells alone was sufficient to induce nephrogenesis from NPs in a bulk co-culture setting without the addition of small molecules or growth factors. This may have resulted from a smaller 'community effect' due to the significantly lower cell mass in our mosaic micro-organoids compared to bulk co-cultures.

Because epithelialized cells are dependent on cell-cell adhesion and cell-substrate adhesion for survival/prevention of death by anoikis, <sup>87</sup> we found that inclusion of 1% Matrigel after pDPAC and selective Rho-kinase inhibitor Y-27632, both during cell patterning and post pDPAC, was critically important to kidney progenitor viability. Similar to previous reports, Y-27632 reduced apoptosis, likely by abrogating membrane blebbing. <sup>88–90</sup>

#### **QUANTIFICATION AND STATISTICAL ANALYSIS**

Unpaired t-tests and one-way analysis of variance (ANOVA) with correction for multiple comparisons using Tukey's honestly significant difference test were performed in Prism 10 software (GraphPad). Trend analyses were conducted through curve fitting using linear and nonlinear least squares regression methods, also performed in Prism 10 software; statistical significance (p values) from the null hypothesis of a line with zero slope were calculated from F tests. Statistical details for each experiment, e.g., the value of n, what n represents, and precision measures, can be found in the results section and/or figure legends. We denote statistical significance with \*p  $\leq 0.05$ , \*\*p  $\leq 0.01$ , \*\*\*p  $\leq 0.001$ , \*\*\*p  $\leq 0.001$ , \*\*\*p  $\leq 0.0001$ .

The Poisson distribution was modeled in Microsoft Excel using the Random Number Generation Analysis Tool, where Poisson mean  $\lambda$  = mean of the experiment distribution.

Cell Systems, Volume 15

### **Supplemental information**

Highly parallel production of designer organoids by mosaic patterning of progenitors

Catherine M. Porter, Grace C. Qian, Samuel H. Grindel, and Alex J. Hughes

#### Supplemental figures

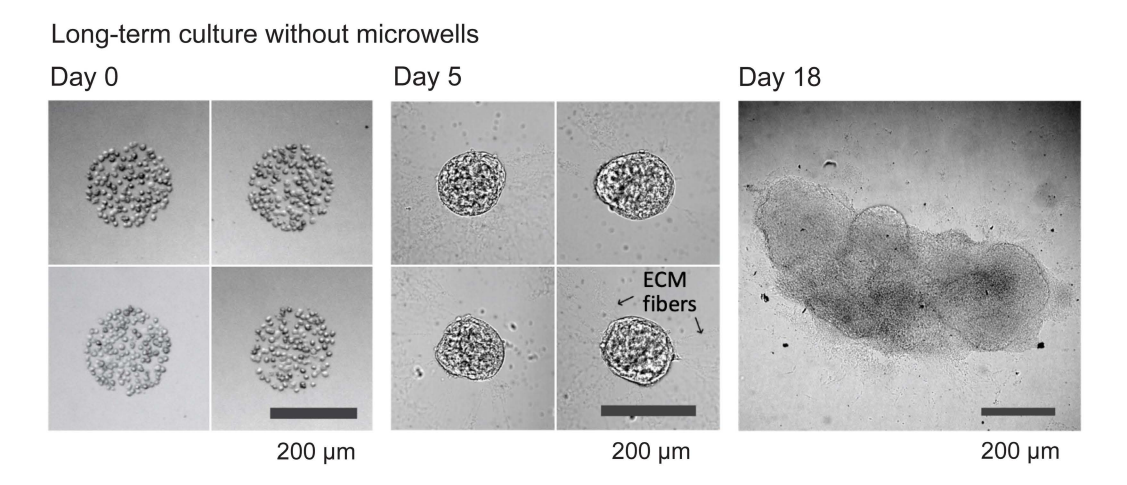


**Fig. S1: Microwells prevent organoid fusion upon extended culture.** Example brightfield micrographs over a differentiation time-course for NP organoids patterned in arrays without microwell walls. Organoids appear to interact with extracellular matrix fibers, drawing neighboring organoids together into large masses over time.

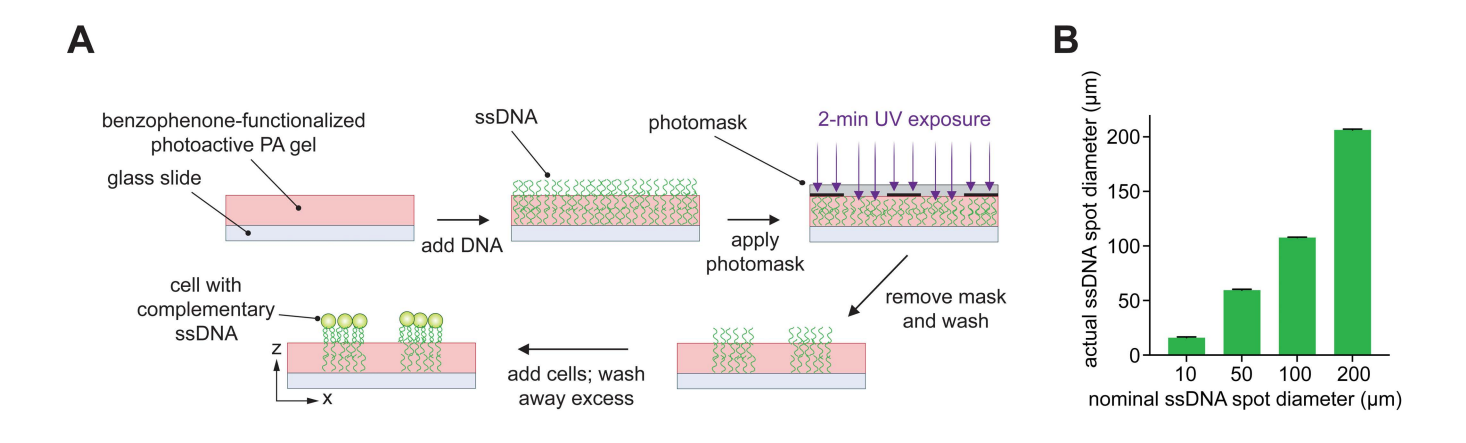
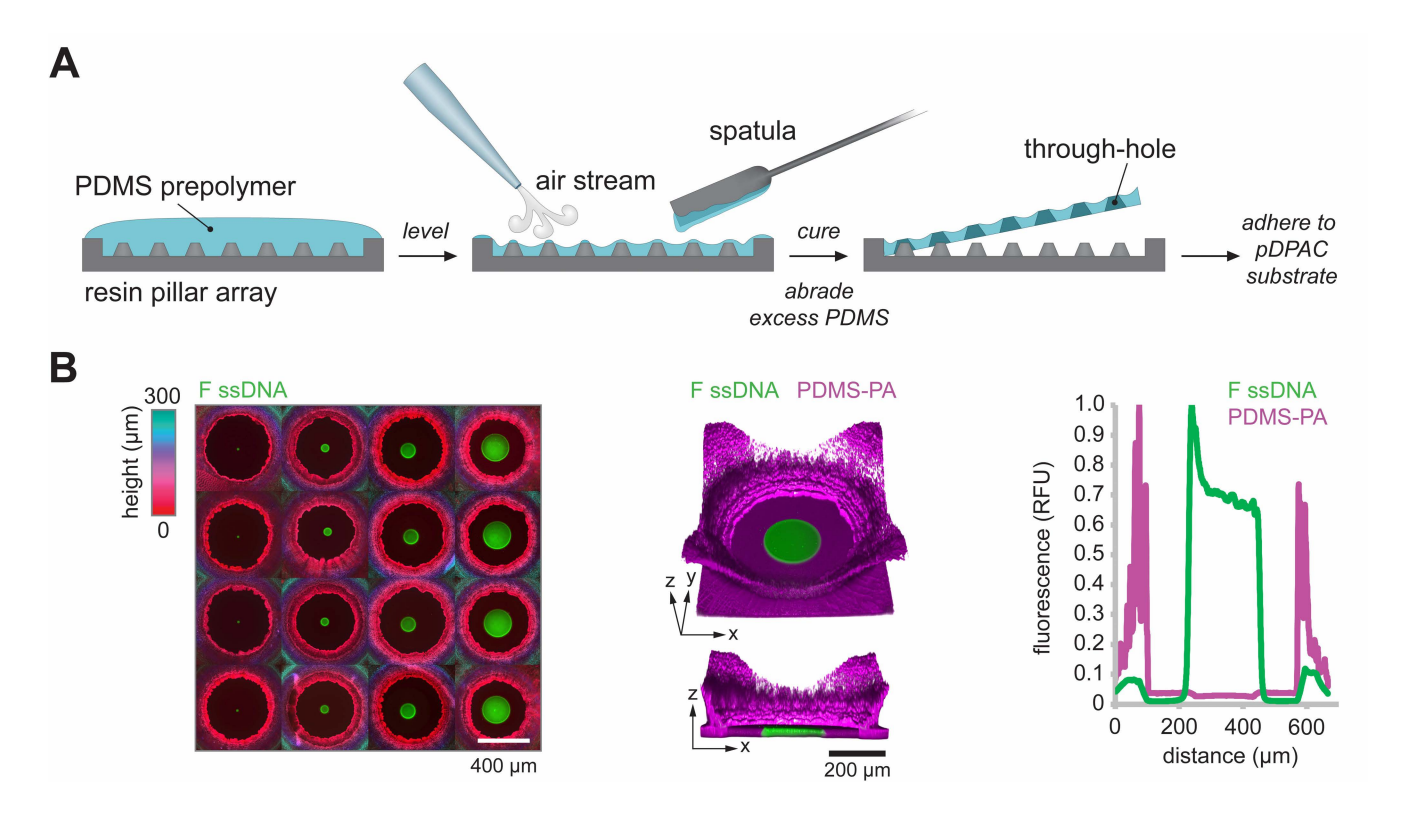
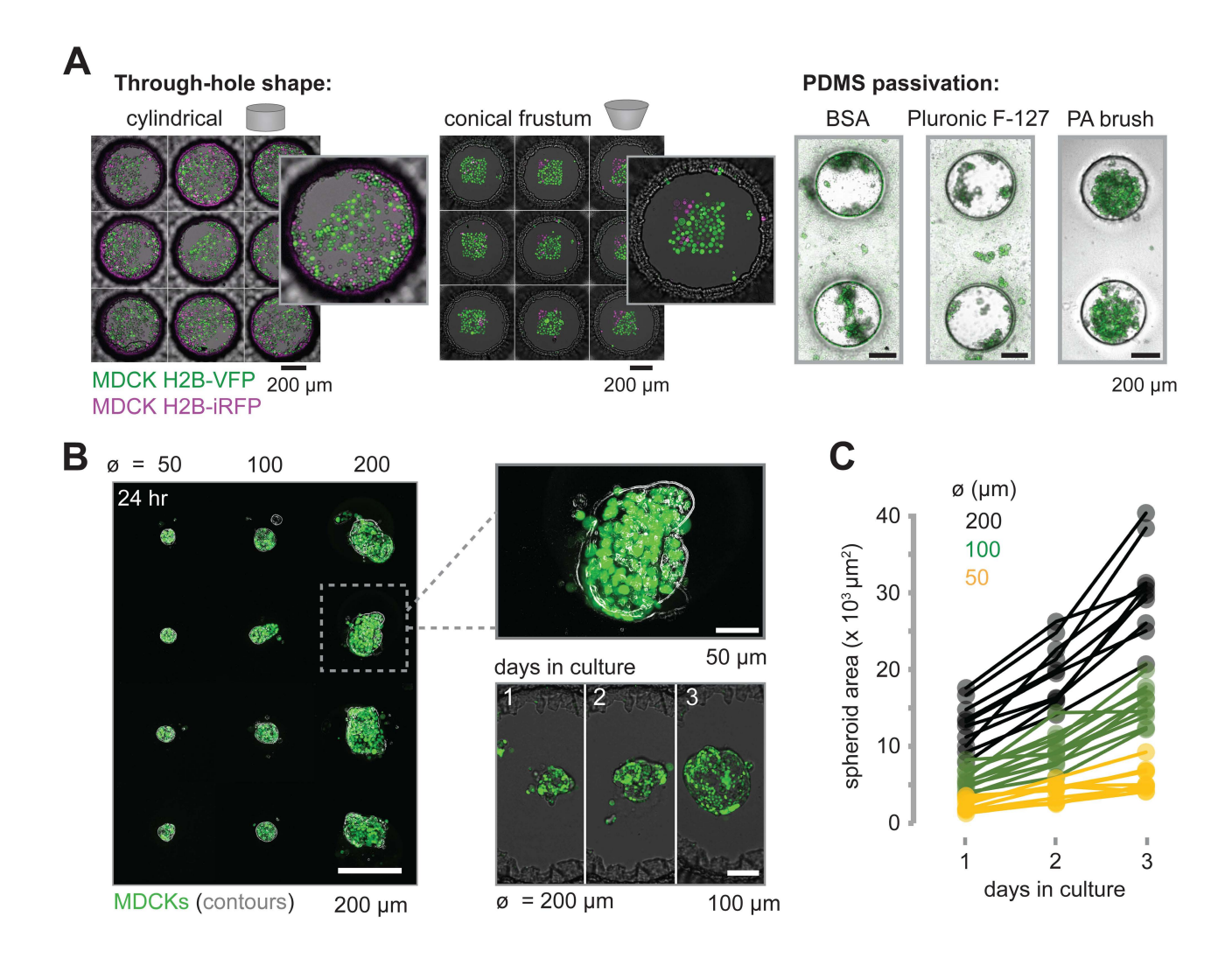


Fig. S2: ssDNA photopatterning is spatially accurate and precise. (A) Schematic of pDPAC: a solution of ssDNA is introduced to a photoactive PA (PPA) gel and patterned using UV light, which passes through a chrome on quartz photomask. Excess ssDNA is washed from the gel. Cells are separately labeled with lipid-conjugated complementary ssDNAs and adhere to the PPA substrate-bound ssDNA pattern. (B) Plot of measured SYBR Gold-labeled 'F' ssDNA spot diameters patterned on PPA substrates vs nominal diameter of corresponding photomask circular spot features (mean  $\pm$  S.D.,  $n \ge 9$  spot patterns per nominal Ø).



**Fig. S3:** Addition of microwell walls and culture chambers for long-term organoid culture. (A) Fabrication of PDMS through-hole sheets by replica micromolding. Resin pillar arrays were 3D-printed using low force stereolithography and then used as a replica mold for PDMS silicone casting. PDMS pre-polymer is poured on a pillar array and leveled with a flat-edged spatula. A stream of compressed air breaks the connection between the pre-polymer on top of the pillars and that which is drawn up the sides of the pillars by capillary action. The PDMS is then cured, discs of silicone are abraded off the tops of pillars, and the molded through-hole sheet is removed from the resin substrate. (**B**) *Left*, confocal fluorescence micrograph montage of ssDNA patterns labeled with SYBR Gold. Height of the PDMS microwell array overlay is encoded by color based on confocal imaging of a rhodamine-methacrylamide co-monomer incorporated into the non-adhesive PA coating. *Middle*, 3D rendering of example ssDNA feature and associated microwell (as in **Fig. 1C**), with, *Right*, corresponding fluorescence profiles of ssDNA and PDMS microwell array coating.



**Fig. S4: Microwell engineering enables long-term 3D culture after precise cell patterning with low non-specific background and adhesion properties.** (**A**) *Left*, conical microwell design reduces non-specific cell patterning. Confocal fluorescence micrographs of typical patterning substrate appearance after performing pDPAC in microwells with PDMS walls having cylindrical or conical profiles. Incomplete and variable washout of non-specifically adhered cells is typically observed for cylindrical wells. *Right*, polyacrylamide brush derivatization of PDMS microwell walls enables robust and long-term blocking of cell adhesion. Confocal fluorescence micrographs of microwells blocked with bovine serum albumin (BSA), Pluronic F-127, or linear polyacrylamide (PA brush), passively seeded with MDCK H2B-VFP cells, and cultured for 3 days. (**B**) *Left*, micrograph montage of MDCK spheroids at 72 hr after patterning in 2D. The montage is a composite with the brightfield channel processed with 'find edges' in FIJI to emphasize spheroid contours. *Right*, micrographs of an example spheroid from a 200 μm ssDNA pattern over the course of three days in culture. (**C**) Growth curves for representative spheroids in each Ø group (*n* = 10 spheroids per Ø).

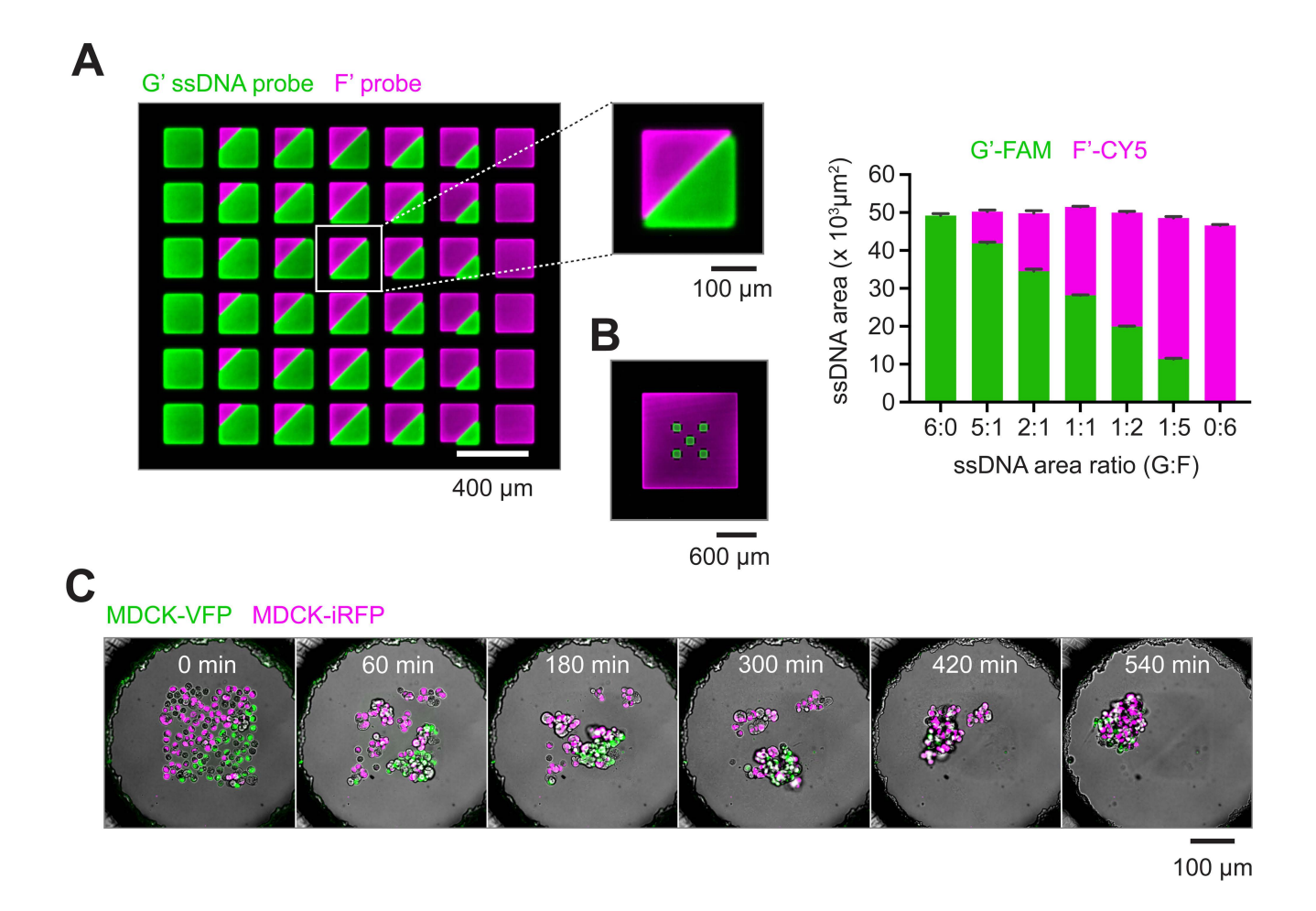


**Fig. S5: Patterns of multiple orthogonal ssDNA sequences enable multiplexing of cell populations, precise ratio control, and 2D-to-3D transition.** (**A**) *Left*, confocal fluorescence micrograph montage of example ssDNA patterns over a range of nominal G and F ssDNA surface area ratios, concatenated from 42 microwells. *Right*, histogram of measured pattern areas (mean  $\pm$  S.D., n = 6 patterns per area ratio) against nominal area ratios (measured from the photomask). (**B**) Confocal fluorescence micrograph of successive ssDNA fiducial patterns on a pDPAC substrate. G ssDNA is patterned first and stained with a G'-FAM probe, creating a crosshair that is positionally aligned with the next photomask for F ssDNA patterning. Simultaneous alignment of similar marks positioned elsewhere on the mask enables rotational alignment. Here, F ssDNA is stained with a F'-CY5 probe. (**C**) Confocal fluorescence micrograph frames taken from **Movie S2** showing a time-lapse of mosaic spheroid condensation following transient patterning on ssDNA.

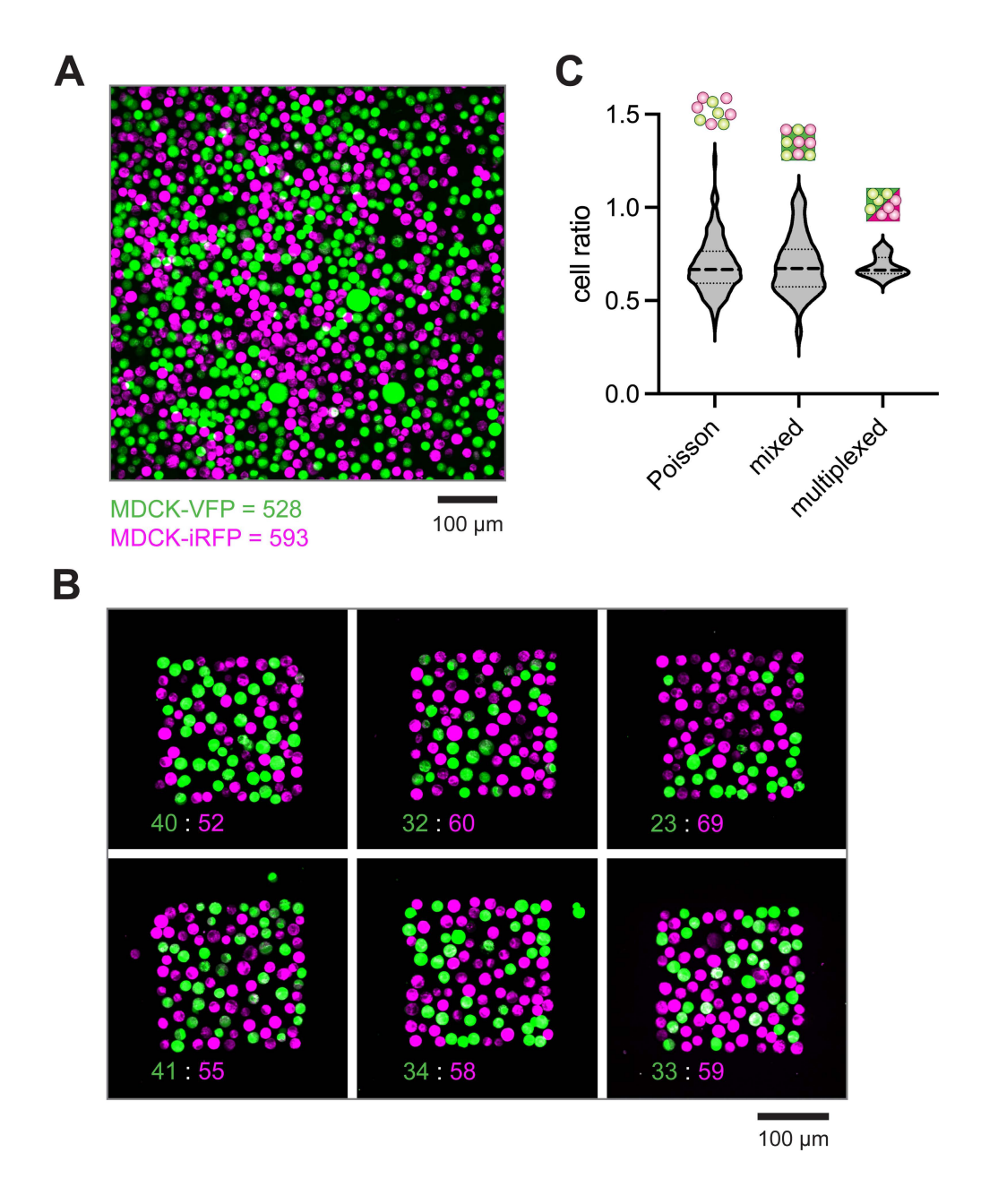


Fig. S6: Patterning premixed cell populations on a single ssDNA sequence increases variance in resulting cell type ratios. (A) Confocal fluorescence micrograph of mixed MDCK-VFP and MDCK-iRFP cells before pDPAC, with a targeted ratio of 1:1 based on cell counts performed prior to mixing. Fluorescence was enhanced using CellTracker dyes, and cells were manually counted/annotated in Fiji. (B) Montage of example fluorescence micrographs of mixed MDCKs in (A) patterned on 200  $\mu$ m x 200  $\mu$ m F ssDNA squares, with manual cell counts below each. Cells not adhered to patterns were excluded from cell counts. (C) Violin plots of cell ratios resulting from 1) two modeled Poisson distributions, where the average cell counts match those in the mixed group ('Poisson', n = 500), 2) ratios of premixed MDCK populations patterned on F ssDNA squares ('mixed', n = 43) as in (B), and 3) ratios of unmixed MDCK populations, patterned sequentially on dual F/G ssDNA squares with a nominal surface area ratio of 1:1 ('multiplexed', n = 10). Within each experimental group, the designated denominators for cell ratio calculations were the cell counts of the MDCK population that had the higher capture efficiency on average.

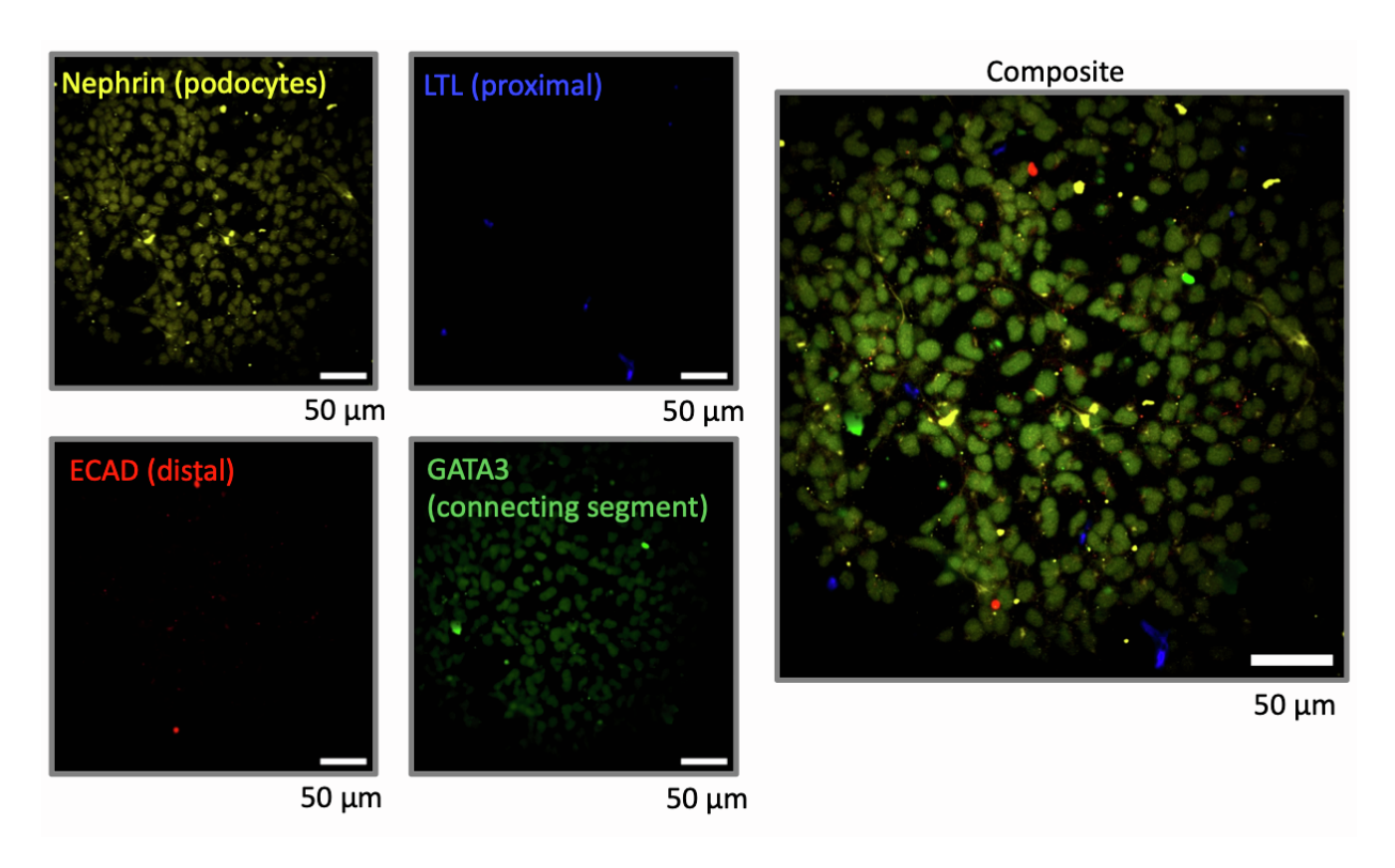


Fig. S7: Patterned nephron progenitors do not yet express markers of early nephron cell lineages. Immunofluorescence micrographs of day 10 iPSC-derived nephron progenitors assayed for expression of the indicated early nephron markers for podocyte, proximal, distal, and connecting segment lineages. All fluorescence profiles are consistent with negative staining.

### passive seeding

cell suspension density

day 10

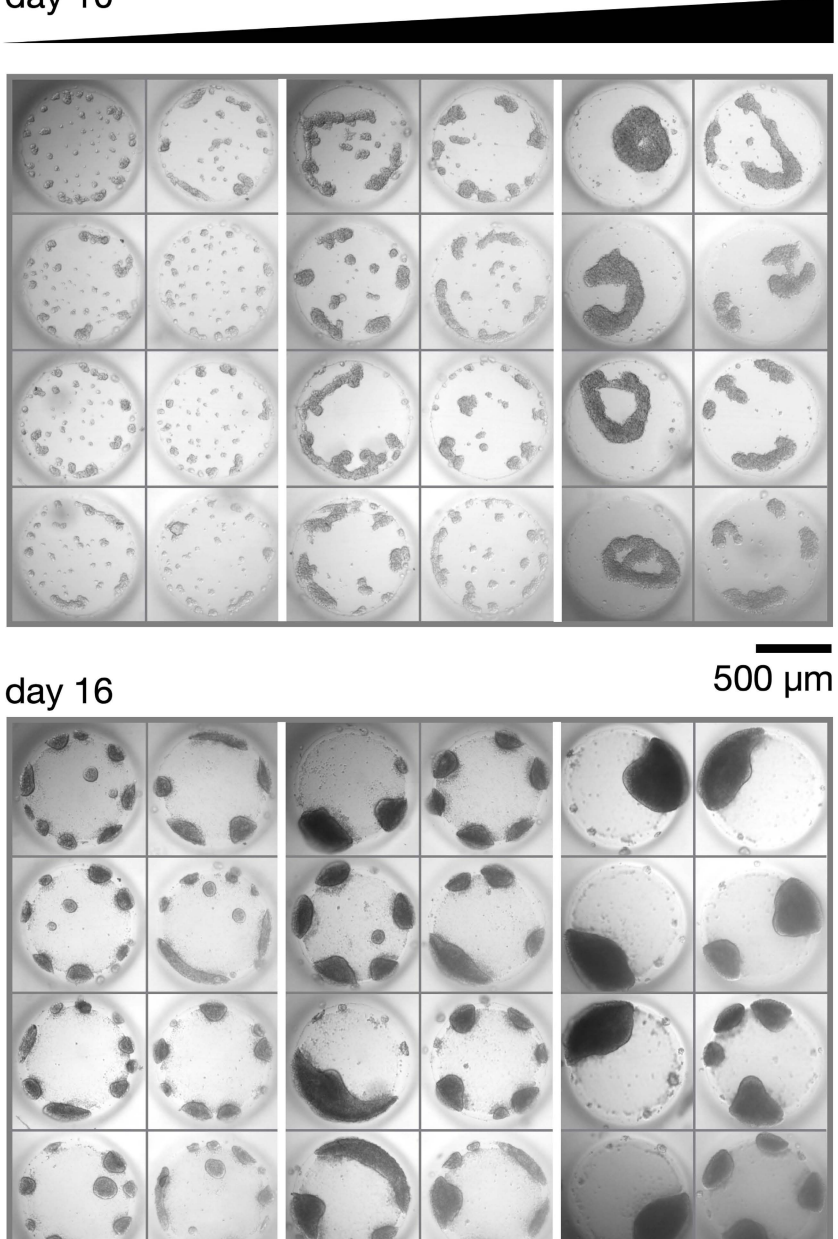
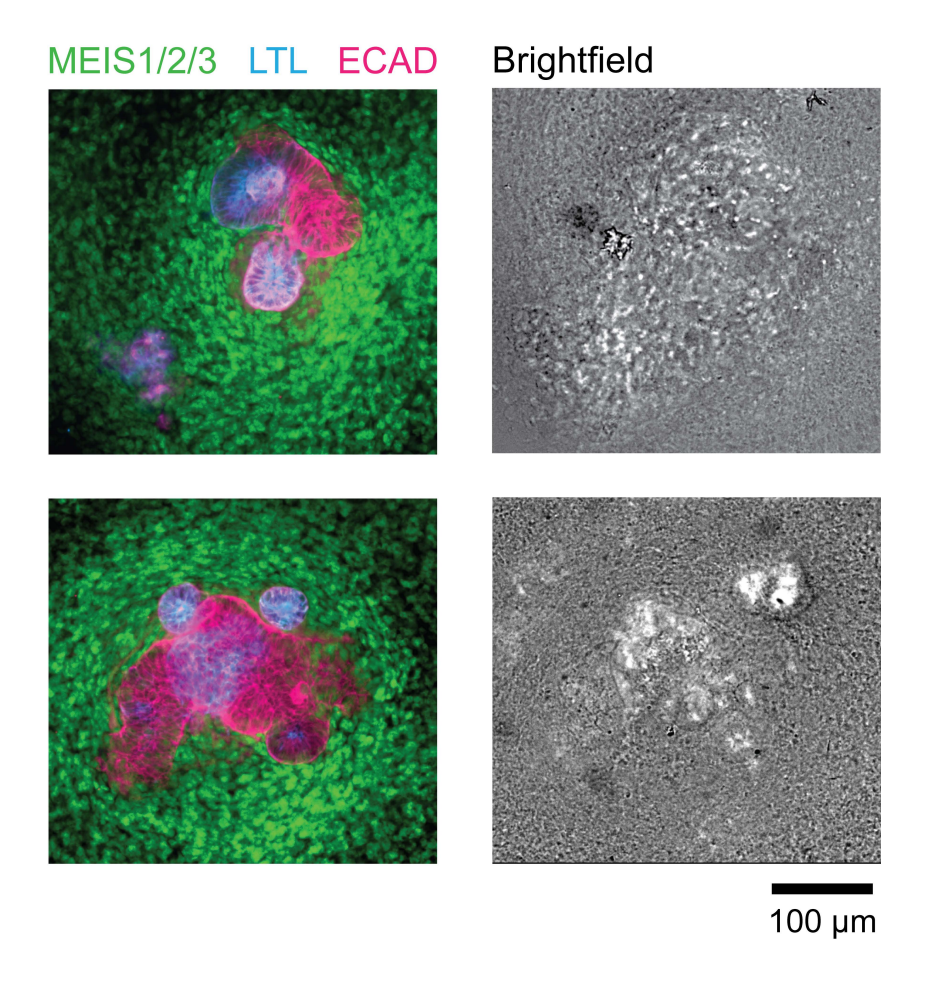
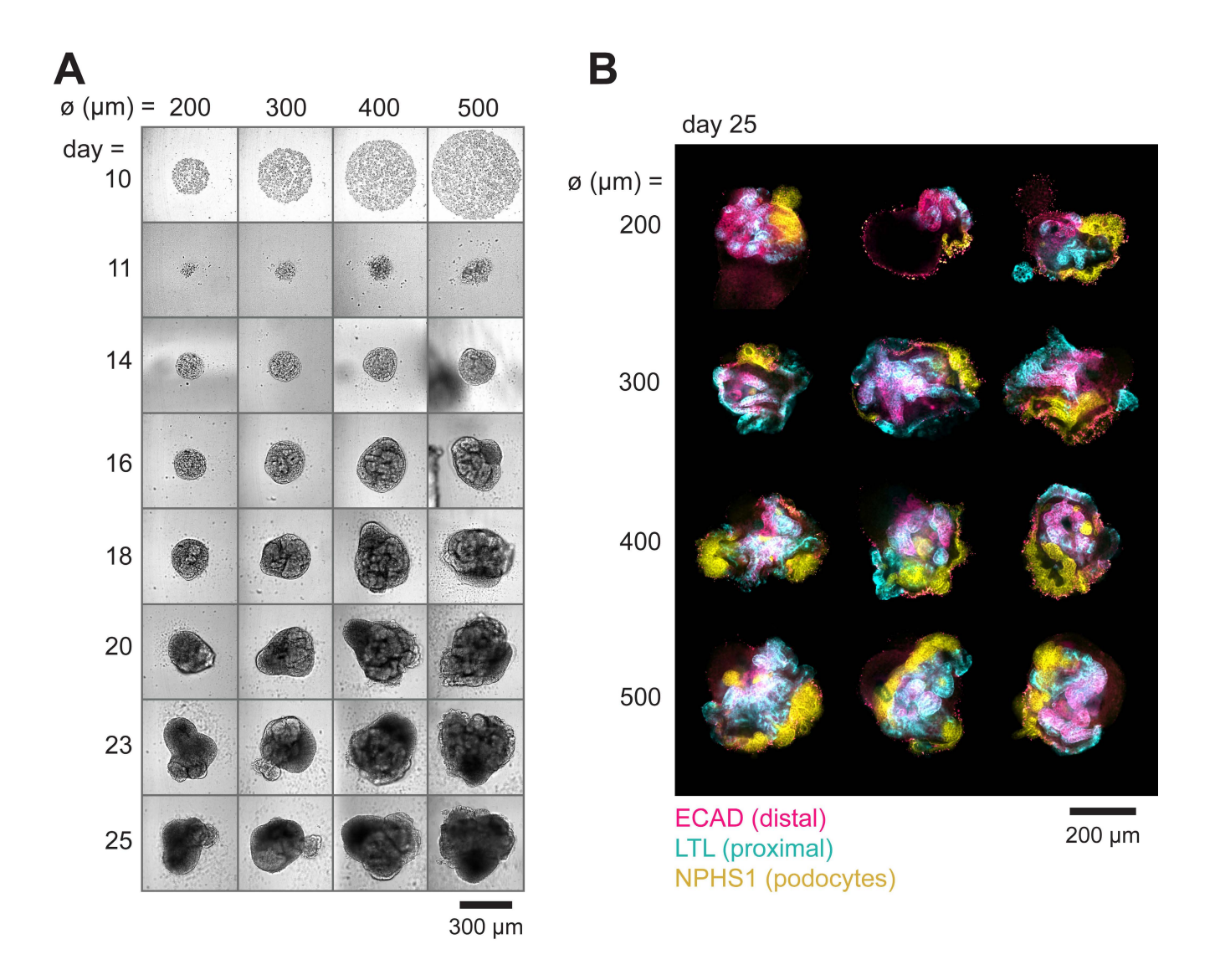


Fig. S8: Passive nephron progenitor seeding rather than cell patterning leads to unpredictable organoid number and size. Brightfield confocal micrographs of microwells lacking ssDNA patterns seeded with nephron progenitors over a range of cell densities  $(0.5, 1, \text{ or } 2x10^5 \text{ cells per chamber of an } 8\text{-chambered slide})$  and imaged 2 hours after seeding and 6 days later.



**Fig. S9: Stromal-like cells surround epithelial structures in organoids.** *Left*, confocal micrographs of nephron organoids, stained for markers of proximal tubule (LTL), distal tubule (ECAD+ LTL-), and stroma (MEIS1/2/3). *Right*, corresponding brightfield confocal micrographs.



**Fig. S10:** pDPAC and nephron organoid differentiation using PENN123i-SV20 hiPSC-derived NPs. (A) Brightfield confocal micrographs during the development of PENN123i-SV20 (ref. <sup>1</sup>)-derived NP organoids, including patterning on circular ssDNA patterns with the indicated diameter Ø on day 10 of differentiation, through to the differentiation endpoint on day 25. (**B**) Micrograph montage of day 25 endpoint nephron organoids, fixed and immunostained for markers of nephron distal tubule (ECAD), proximal tubule (LTL), and podocytes (NPHS1), with 3 examples for each ssDNA spot diameter Ø.

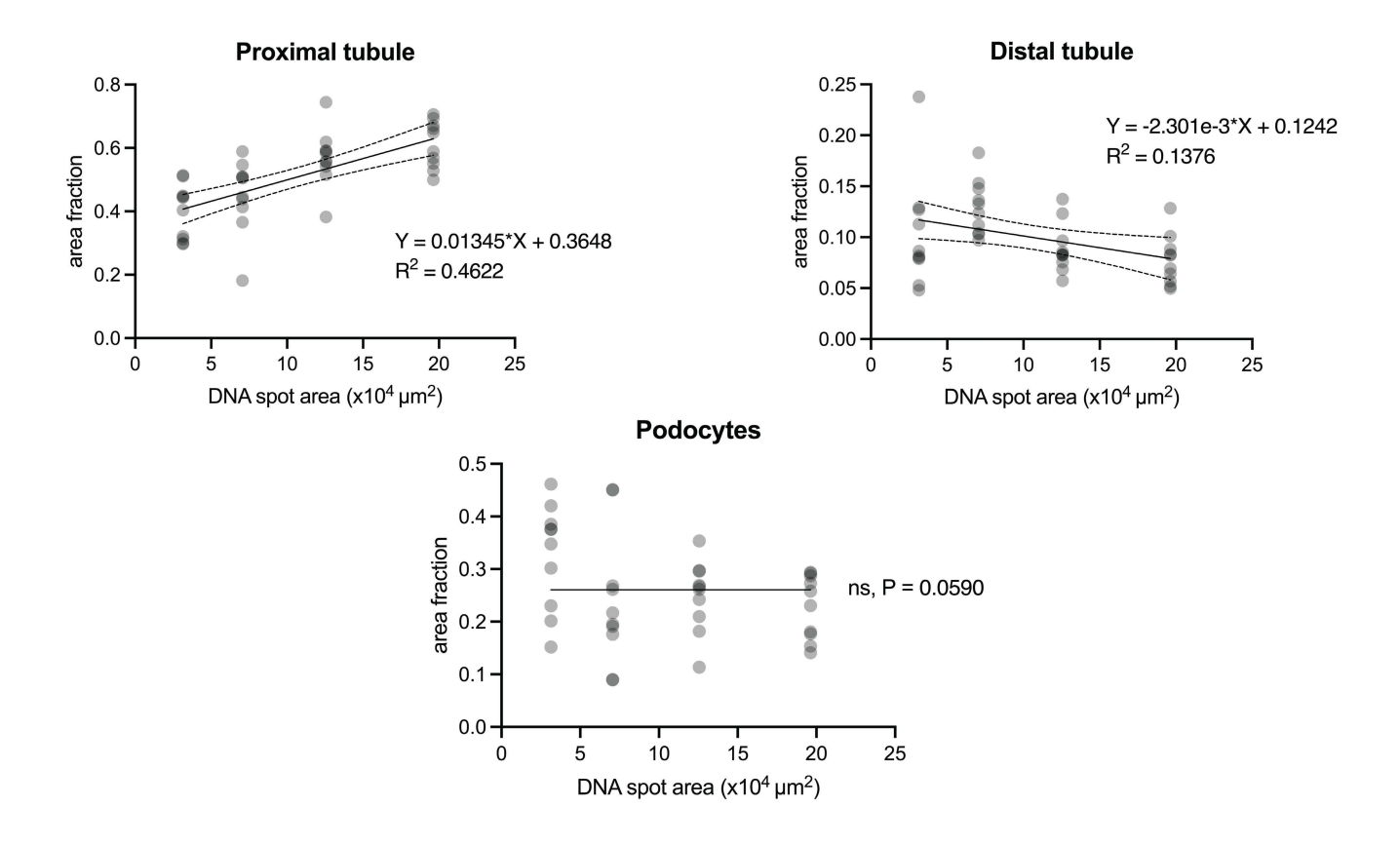


Fig. S11: With increasing initial numbers of NPs, proximal tubule proportions increase and distal tubule proportions decrease in organoids. Results of curve fitting using least squares linear and nonlinear regression methods for proximal tubule, distal tubule, and podocyte tissue proportions in organoids at 15 days post cell patterning. Both proximal and distal tubule tissue segmentation data have sloped lines of best fit with statistical significance from zero (F test, proximal p < 0.0001, distal p = 0.019), whereas podocyte data fits better to a horizontal line (n = 10 organoids per DNA spot size).

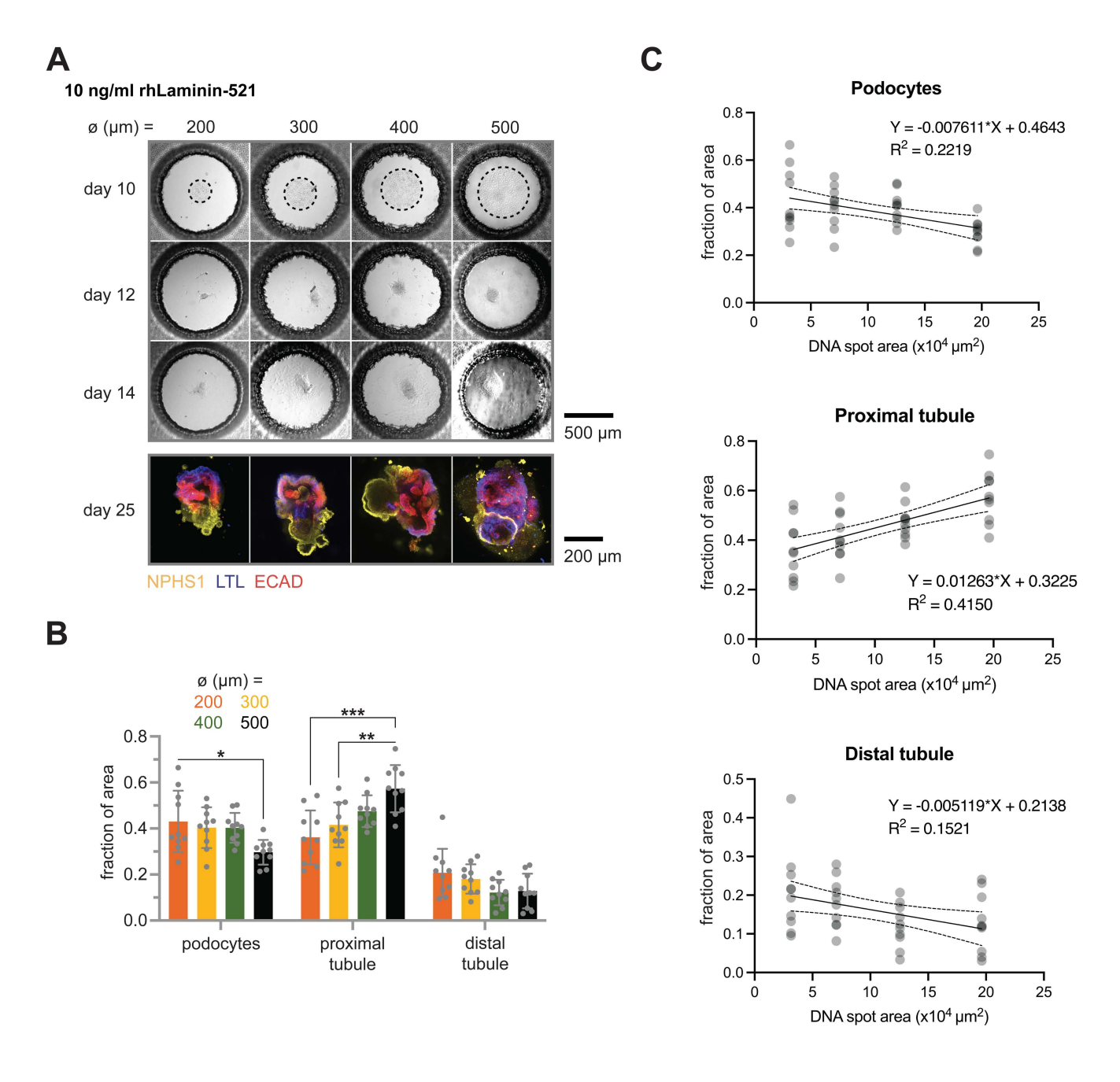
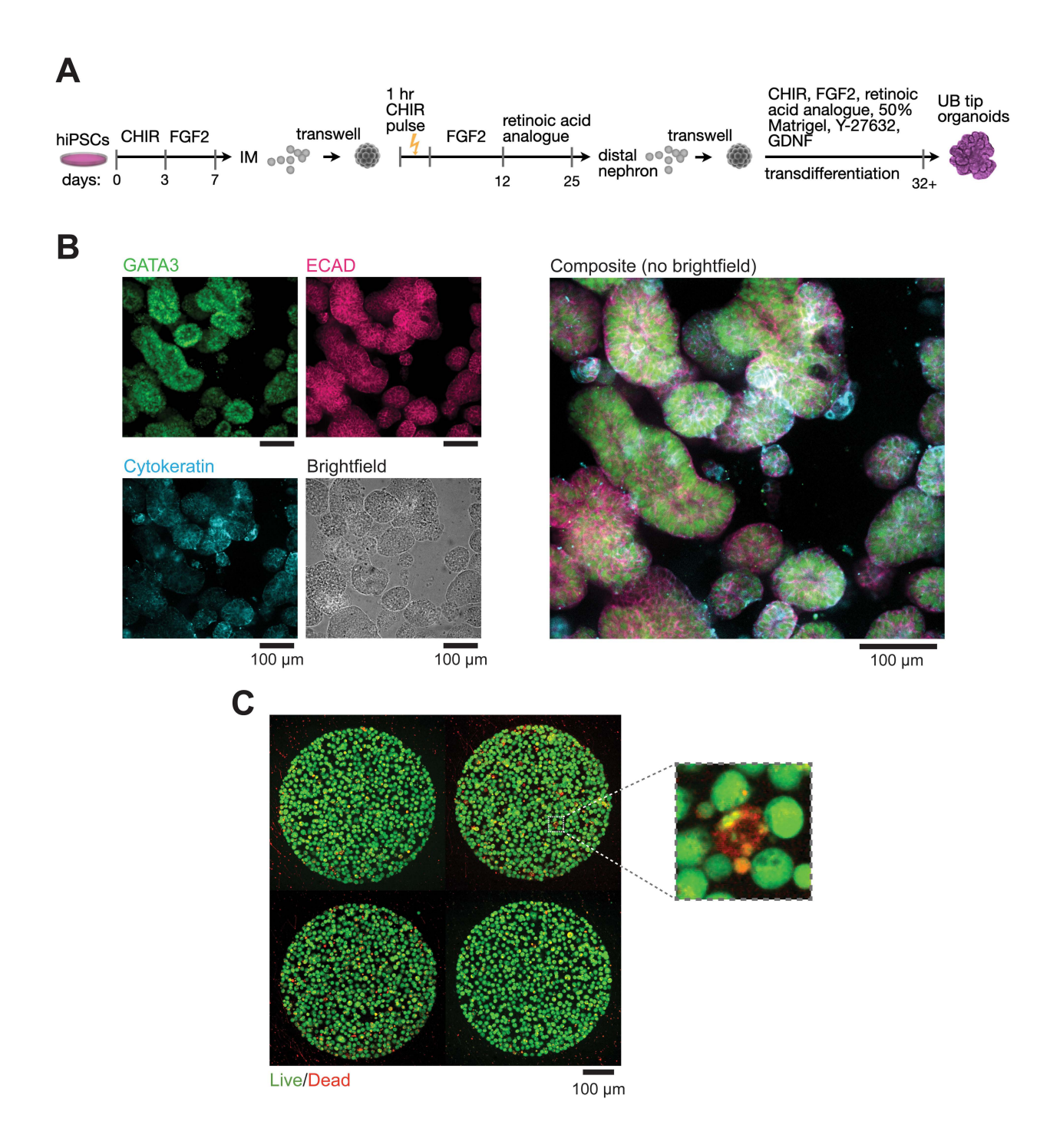


Fig. S12: Similar aggregation and size- and composition-controlled organoid formation for recombinant human laminin culture conditions. (A) Representative brightfield and immunofluorescence confocal micrographs during differentiation of nephron progenitor organoids in 10 ng/ml rhLaminin-521 media after patterning on circular ssDNA patterns with the indicated diameter  $\emptyset$ . Dotted lines emphasize the extent of 2D cell patterns prior to transition to 3D culture. (B) Plot of organoid composition (ratio of cell type area to total area of all cell types measured, mean  $\pm$  S.D., 3 slices per n = 10 organoids per  $\emptyset$ , Tukey's multiple comparisons test, \*p  $\le$  0.05, \*\*p  $\le$  0.01, \*\*\*p  $\le$  0.001). (C) Trend analysis results of curve fitting using least squares linear and nonlinear regression methods for proximal tubule, distal tubule, and podocyte tissue proportions in day 25 endpoint organoids. Segmentation data for all immunostained tissue types have sloped lines of best fit with statistical significance from zero (F test, podocytes p = 0.0022, proximal p < 0.0001, distal p = 0.0128).



**Fig. S13:** hiPSC-derived UB tip cells have appropriate identity markers, pDPAC patterning, and viability after patterning. (A) Schematic of hiPSC differentiation to intermediate mesoderm (IM), followed by differentiation to distal nephron epithelium and transdifferentiation to UB tip-like cells.<sup>2</sup> (**B**) Brightfield and immunofluorescence confocal micrograph of UB tip organoids, stained for markers consistent with UB identity, including GATA3 (green), ECAD (bright pink), and cytokeratin (cyan). (**C**) Montage of example confocal fluorescence micrographs of UB tip cells assayed for viability post pDPAC on G ssDNA spots with diameters Ø of 500 μm. Inset shows a dead red cell with green puncta, surrounded by predominantly green live cells.

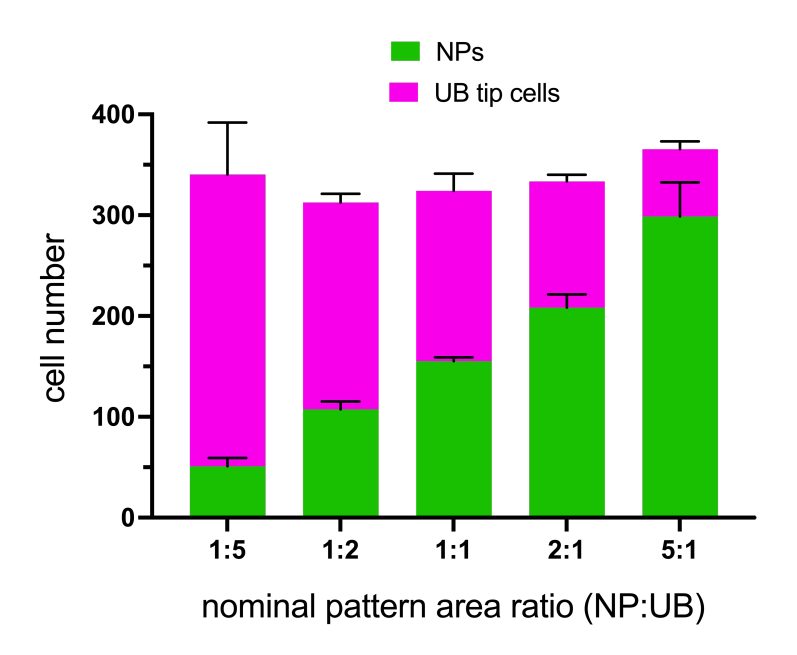


Fig. S14: Dual NP and UB tip cell patterning closely matches nominal ssDNA area ratios. Histogram of NPs and UB tip cells patterned on square, 300  $\mu$ m ssDNA patterns at 5 different nominal area ratios. NPs were patterned on F ssDNA and UB tip cells were patterned on G ssDNA (mean  $\pm$  S.D.,  $n \ge 4$  patterns per area ratio).

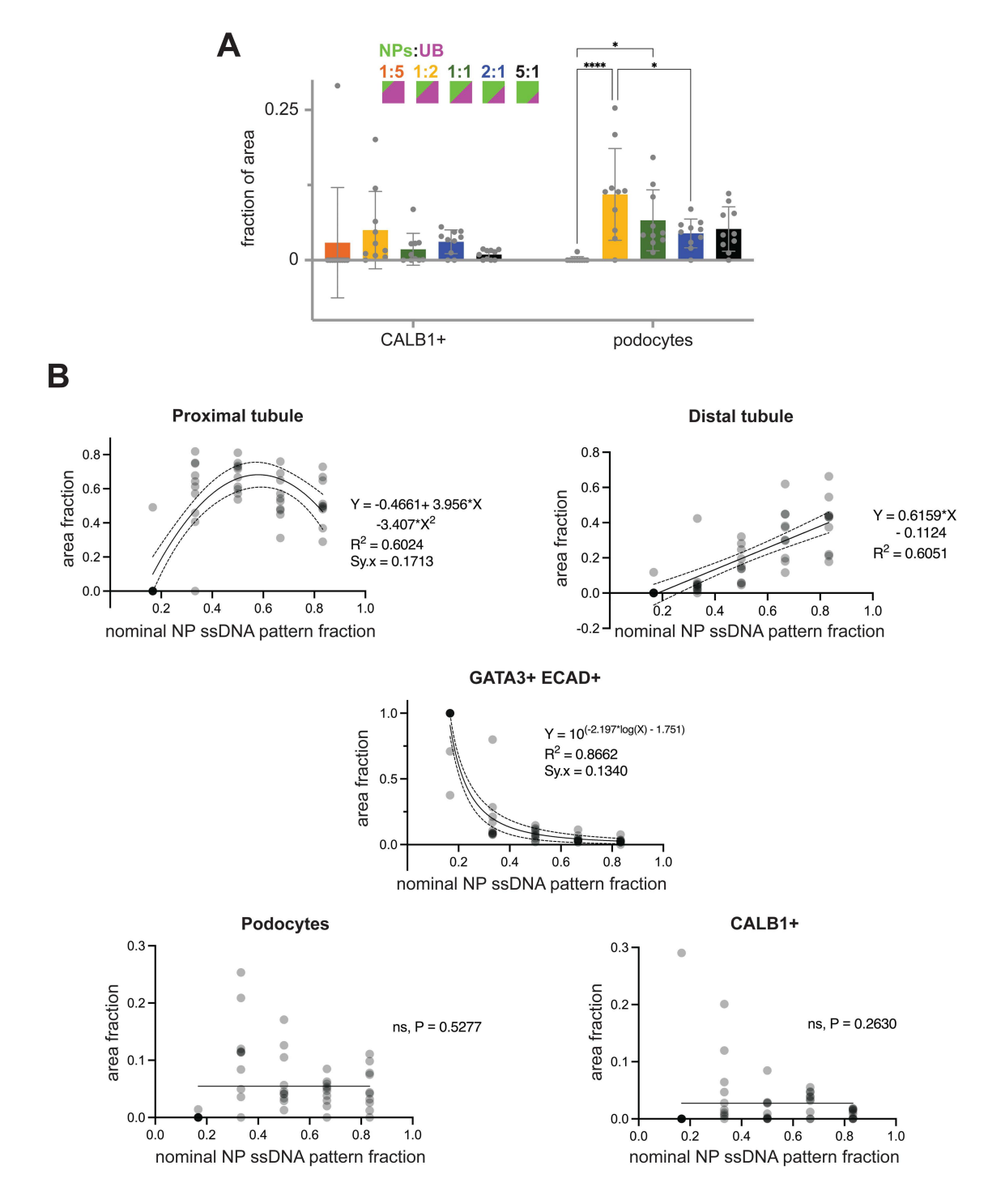


Fig. S15: Proximal tubule, distal tubule, and GATA3+ ECAD+ proportions in mosaic NP/UB tip cell organoids depend on initial progenitor ratios. (A) Plot of mosaic organoid CALB1+ and NPHS1+ podocyte tissues (ratio of cell type area to total area of all cell types measured) for organoids formed from 2D co-patterns of different NP:UB tip cell ratios (mean  $\pm$  S.D., 1-8 slices per n = 10 organoids per ratio, Tukey's multiple comparisons test, \*p  $\leq$  0.05, \*\*p  $\leq$  0.01, \*\*\*p  $\leq$  0.001, \*\*\*\*p  $\leq$  0.0001). (B) Results of curve fitting using least squares regression methods for proximal tubule, distal tubule, GATA3+ ECAD+ tissue, podocyte tissue, and CALB1+ tissue proportions in mosaic organoids at 16 days post cell patterning. Distal tubule tissue segmentation data fit a linear model with a slope having statistical significance from zero (F test, p  $\leq$  0.0001). Proximal tubule and GATA3+ ECAD+ data fit best to nonlinear models and have statistical significance from the null hypothesis of a line with zero slope (extra sum-of-squares F test, p  $\leq$  0.0001 for both). Podocyte and CALB1+ data are consistent with the null hypothesis of a horizontal line (n = 10 organoids per ratio pattern).

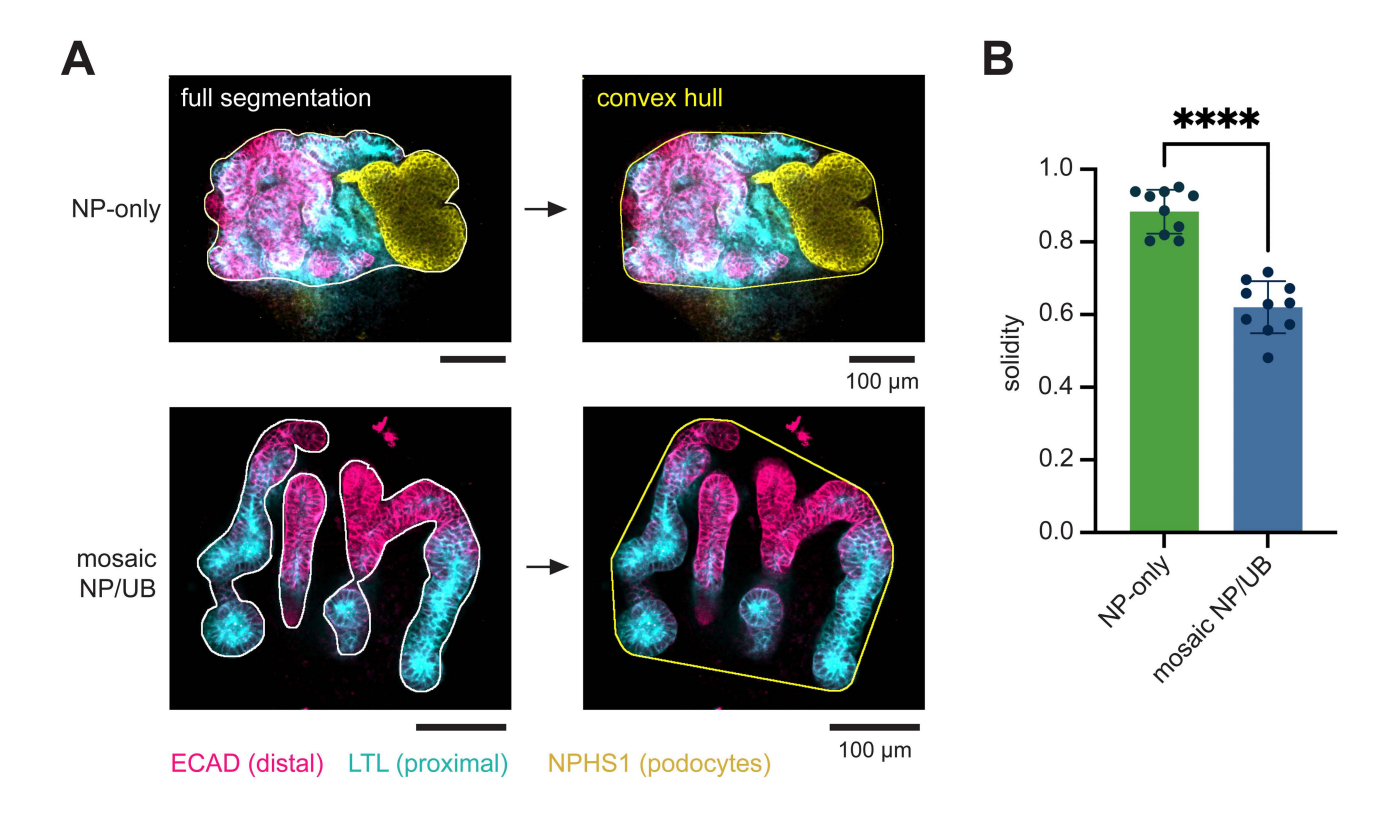


Fig. S16: Mosaic NP/UB tip cell organoids display higher separation of epithelial structures by interdigitating stromal cells relative to NP-only organoids. (A) Representative confocal fluorescence micrographs of the approximate midplanes of an immunostained NP-only organoid, initially patterned on an F ssDNA spot with diameter  $\emptyset$  of 500  $\mu$ m (Top), and a mosaic NP/UB tip cell organoid, patterned on a nominal 2:1 NP:UB tip cell/F ssDNA:G ssDNA patterning ratio (Bottom). Left, white outlines the full manual segmentation of the epithelialized structures and Right, yellow outlines the corresponding convex hulls, annotated/measured in Fiji. (B) Graph of solidity of epithelialized structures (ratio of total area of segmented epithelial structures to convex hull area) of NP-only vs mosaic NP/UB tip cell organoids, as in (A) (mean  $\pm$  S.D., n = 10 organoids per condition, unpaired t test, \*\*\*\*p  $\leq$  0.0001).

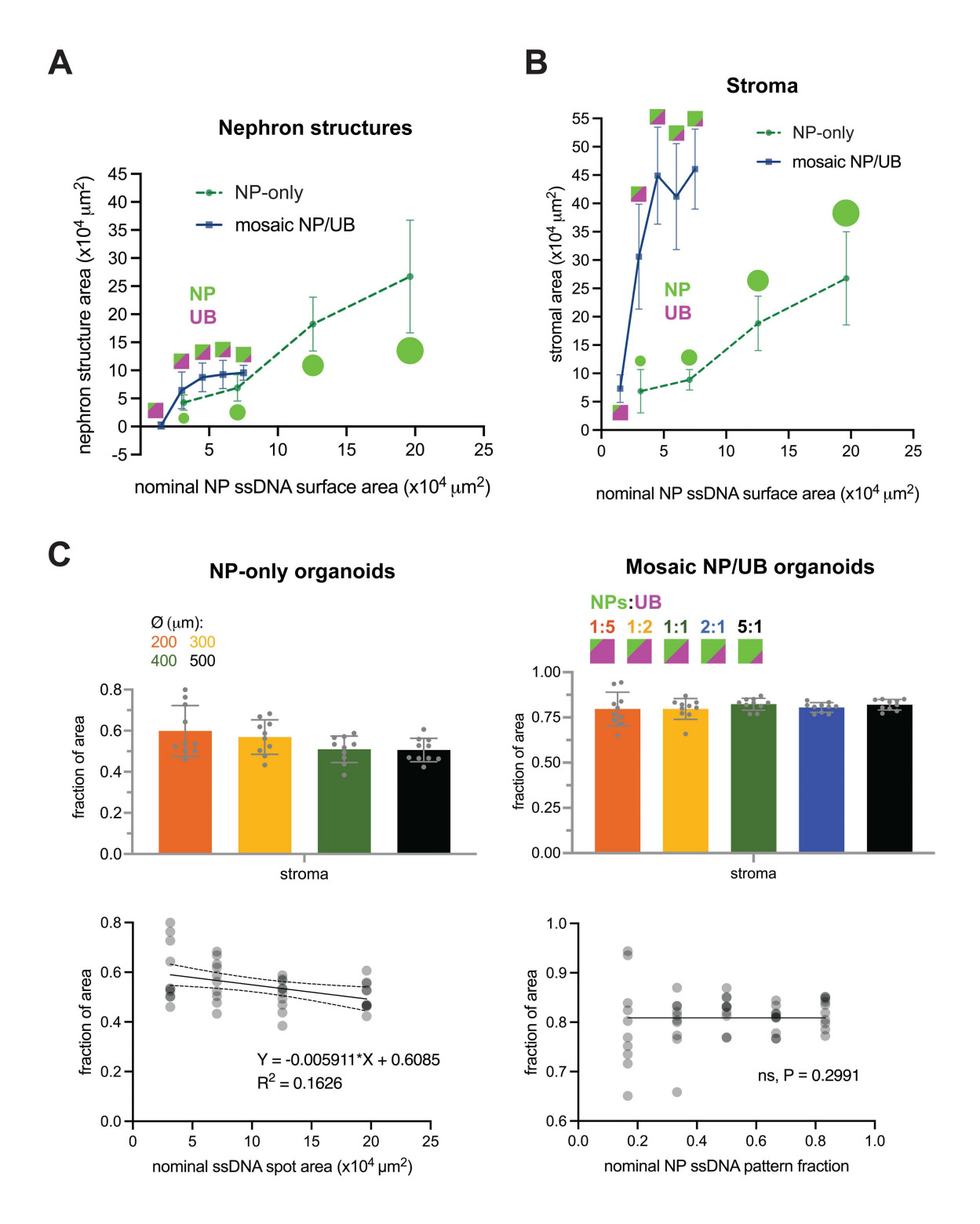


Fig. S17: Mosaic NP/UB tip cell organoids have higher proportions of nephron and stromal tissues relative to NP-only organoids. (A) Total segmented nephron structures in endpoint immunostained NP-only and mosaic NP/UB tip cell organoids based on the initial nominal NP patterning surface area (mean  $\pm$  S.D., 1-8 slices per n = 10 organoids per  $\emptyset$  or ratio). Pictographs above each data point represent initial pDPAC conditions (green, NP, and purple, UB). (B) Total segmented stromal area, corresponding to the endpoint NP-only and mosaic NP/UB tip cell organoids in (A). (C) Plots of overall stromal proportions (Top) for segmented NP-only (Left) and mosaic NP/UB tip cell organoids (Right) from (A) and (B). Bottom, trend analysis results of curve fitting using least squares linear and nonlinear regression methods for stromal proportions in endpoint organoids. The line of best fit for the stromal proportions of NP-only organoids has a slope with statistical significance from zero (F test, p = 0.0099).

#### Supplemental references

- 1. Pashos, E.E., Park, Y., Wang, X., Raghavan, A., Yang, W., Abbey, D., Peters, D.T., Arbelaez, J., Hernandez, M., Kuperwasser, N., et al. (2017). Large, Diverse Population Cohorts of hiPSCs and Derived Hepatocyte-like Cells Reveal Functional Genetic Variation at Blood Lipid-Associated Loci. Cell Stem Cell *20*, 558-570.e10.
- 2. Howden, S.E., Wilson, S.B., Groenewegen, E., Starks, L., Forbes, T.A., Tan, K.S., Vanslambrouck, J.M., Holloway, E.M., Chen, Y.-H., Jain, S., et al. (2021). Plasticity of distal nephron epithelia from human kidney organoids enables the induction of ureteric tip and stalk. Cell Stem Cell 28, 671-